ChemComm

Chemical Communications

rsc.li/chemcomm

ROYAL SOCIETY
OF **CHEMISTRY**
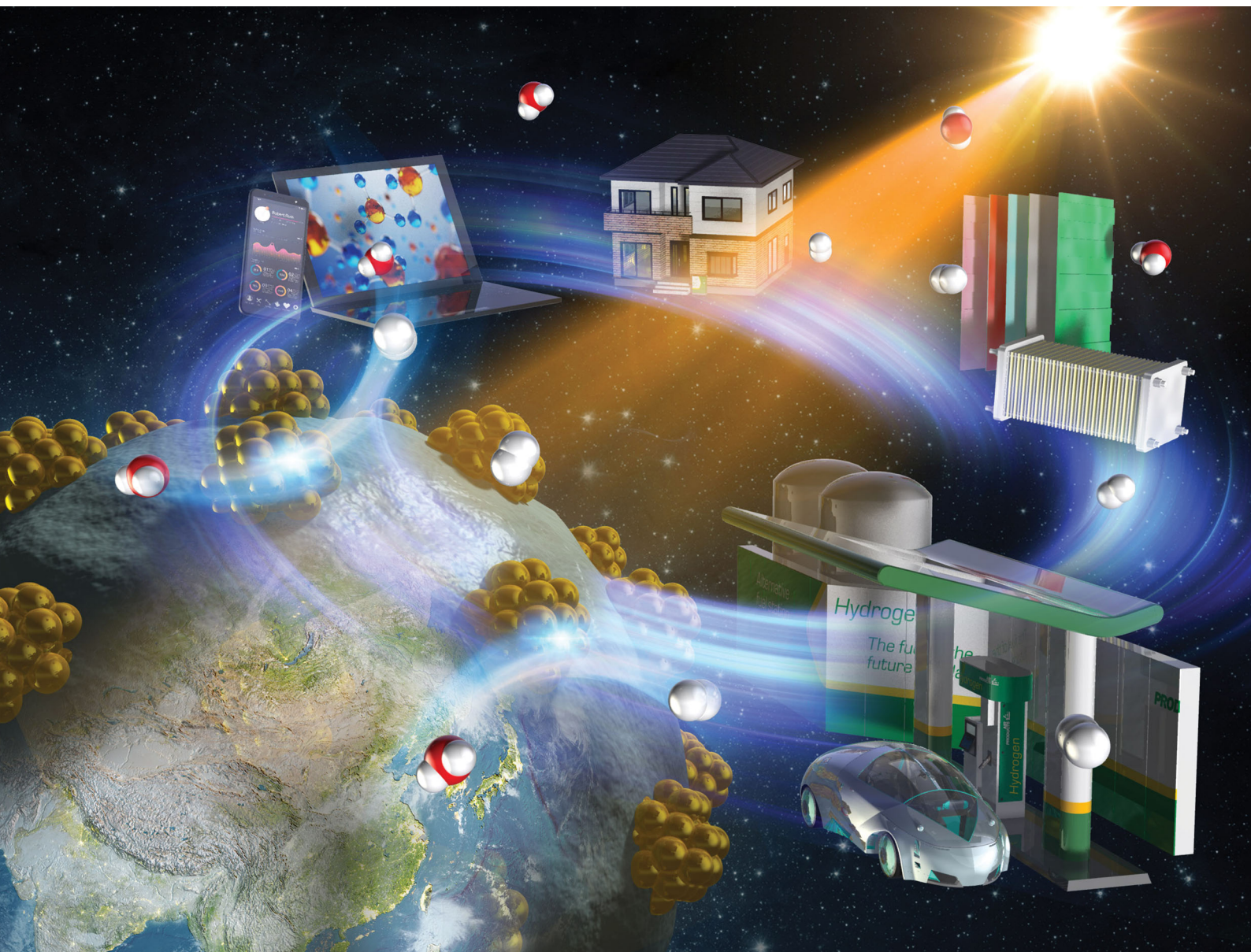
FEATURE ARTICLE
Yuichi Negishi *et al.*
Creation of active water-splitting photocatalysts by
controlling cocatalysts using atomically precise metal
nanoclusters

Creation of active water-splitting photocatalysts by controlling cocatalysts using atomically precise metal nanoclusters

Tokuhisa Kawawaki, [ID] [abc] Yuki Kataoka,[a] Shuhei Ozaki,[a] Masanobu Kawachi,[a] Momoko Hirata[a] and Yuichi Negishi [ID] *[abc]

With global warming and the depletion of fossil resources, our fossil-fuel-dependent society is expected to shift to one that instead uses hydrogen (H_2) as clean and renewable energy. Water-splitting photocatalysts can produce H_2 from water using sunlight, which are almost infinite on the earth. However, further improvements are indispensable to enable their practical application. To improve the efficiency of the photocatalytic water-splitting reaction, in addition to improving the semiconductor photocatalyst, it is extremely effective to improve the cocatalysts (loaded metal nanoclusters, NCs) that enable the reaction to proceed on the photocatalysts. We have thus attempted to strictly control metal NCs on photocatalysts by introducing the precise-control techniques of metal NCs established in the metal NC field into research on water-splitting photocatalysts. Specifically, the cocatalysts on the photocatalysts were controlled by adsorbing atomically precise metal NCs on the photocatalysts and then removing the protective ligands by calcination. This work has led to several findings on the electronic/geometrical structures of the loaded metal NCs, the correlation between the types of loaded metal NCs and the water-splitting activity, and the methods for producing high water-splitting activity. We expect that the obtained knowledge will lead to clear design guidelines for the creation of practical water-splitting photocatalysts and thereby contribute to the construction of a hydrogen-energy society.

[a] *Department of Applied Chemistry, Faculty of Science, Tokyo University of Science, Kagurazaka, Shinjuku-ku, Tokyo 162-8601, Japan. E-mail: negishi@rs.tus.ac.jp*

[b] *Research Institute for Science and Technology, Tokyo University of Science, Kagurazaka, Shinjuku-ku, Tokyo 162-8601, Japan*

[c] *Photocatalysis International Research Center, Tokyo University of Science, 2641 Yamazaki, Noda, Chiba 278-8510, Japan*
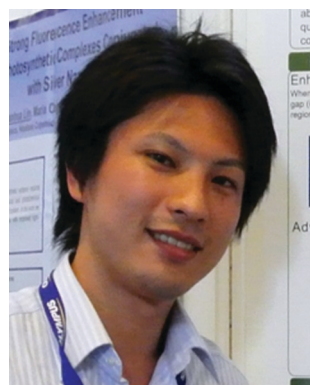
Tokuhisa Kawawaki

Tokuhisa Kawawaki Assistant Professor of the Department of Applied Chemistry at Tokyo University of Science. He received a PhD degree (2015) in Applied Chemistry from the University of Tokyo. In 2016–2017, he worked as a Japan Society for the Promotion of Science (JSPS) Postdoctoral fellow (PD) at the University of Melbourne. In 2017–2018, he worked as a JSPS super PD (SPD) at Kyoto University. In 2019, he moved to his current position. His current research topics include the synthesis of metal nanoparticles and nanoclusters in solution and their applications for photoelectrochemistry and photocatalysts.

Yuki Kataoka

Yuki Kataoka Master course student in the Negishi group at Tokyo University of Science. He received a BSc (2019) in Chemistry from Tokyo University of Science. His research interests include the activation of water-splitting photocatalysts by heteroatom doping of cocatalysts and elucidation of the calcination process for loading precise metal NCs on photocatalysts.

1. Introduction

1.1. Background

In the 21st century, humankind is facing unprecedented serious energy and environmental issues such as the depletion of fossil resources and the destruction of the environment on a global scale.[1] Thus, it is expected to address these problems to create a sustainable society as soon as possible. The energy conversion system shown in Fig. 1 is one of the ultimate systems for constructing such a society.[2] In this system, hydrogen (H_2) is produced by a photocatalyst[3] and/or an electrolysis cell,[4–15] and the obtained H_2 is converted into electric power by a fuel cell.[16–24] With such a system, it is possible to obtain energy from water and sunlight, which are almost infinite on the earth. In addition, when this system is used, the energy medium (H_2) can be circulated, preventing the problem of energy depletion. Furthermore, carbon dioxide (CO_2), which leads to global warming, is not generated in this system. For constructing this system, modern chemistry is expected to improve the functionality of the photocatalysts, electrolysis cells, and fuel cells.

1.2. Water-splitting photocatalysts

For H_2 production, photocatalytic reactions (Fig. 1) can produce H_2 directly from water and sunlight.[25–37] Therefore, the photocatalytic water-splitting reaction is considered to be one of the cleanest energy-production reactions for humankind. Among the materials that enable such a reaction to proceed, powder semiconductor photocatalysts have the advantages of a simple system and the ease of increasing the surface area. Because of these advantages, if a large-scale H_2-production plant using a powder semiconductor photocatalyst is constructed in a desert or uninhabited island where sunlight is abundant, a large amount of H_2 is expected to be generated.[38] However, currently, the solar-to-hydrogen (STH) conversion efficiency is only 1.1%.[39] To enable practical use of a water-splitting photocatalyst, it is indispensable to improve the STH conversion efficiency to approximately 5–10%.[33]

When a semiconductor photocatalyst is used, H_2 and oxygen (O_2) are produced from water via the following three processes:[25] (i) excitation of electrons from the valence band (VB) to the conduction band (CB) of the photocatalyst by light irradiation, (ii) charge transfer of excited electrons and holes
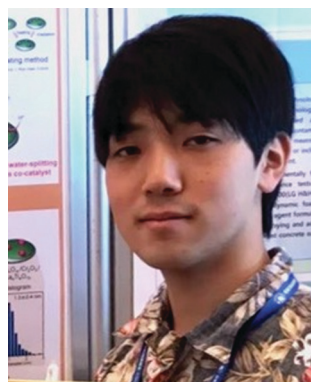
Shuhei Ozaki Master course student in the Negishi group at Tokyo University of Science. He received a BSc (2019) in Chemistry from Tokyo University of Science. In 2019, he worked as a study abroad student at The University of Adelaide (Greg Metha's group). His research interests include the activation of visible-light-driven water-splitting photocatalysts.

Shuhei Ozaki

Masanobu Kawachi Master course student in the Negishi group at Tokyo University of Science. He received a BSc (2020) in Chemistry from Tokyo University of Science. His research interests include the activation of visible-light-driven water-splitting photocatalysts.

Masanobu Kawachi

Momoko Hirata Master course student in the Negishi group at Tokyo University of Science. She received a BSc (2020) in Chemistry from Tokyo University of Science. Her research interests include the elucidation of the calcination process for loading precise metal NCs on photocatalysts.

Momoko Hirata

Yuichi Negishi Professor of the Department of Applied Chemistry at Tokyo University of Science. He received a PhD degree in Chemistry in 2001 under the supervision of Prof. Atsushi Nakajima from Keio University. Before joining Tokyo University of Science in 2008, he was employed as an Assistant Professor at Keio University and at the Institute for Molecular Science. His current research interests include the precise

Yuichi Negishi

synthesis of stable and functionalized metal nanoclusters and their applications in energy and environmental materials.
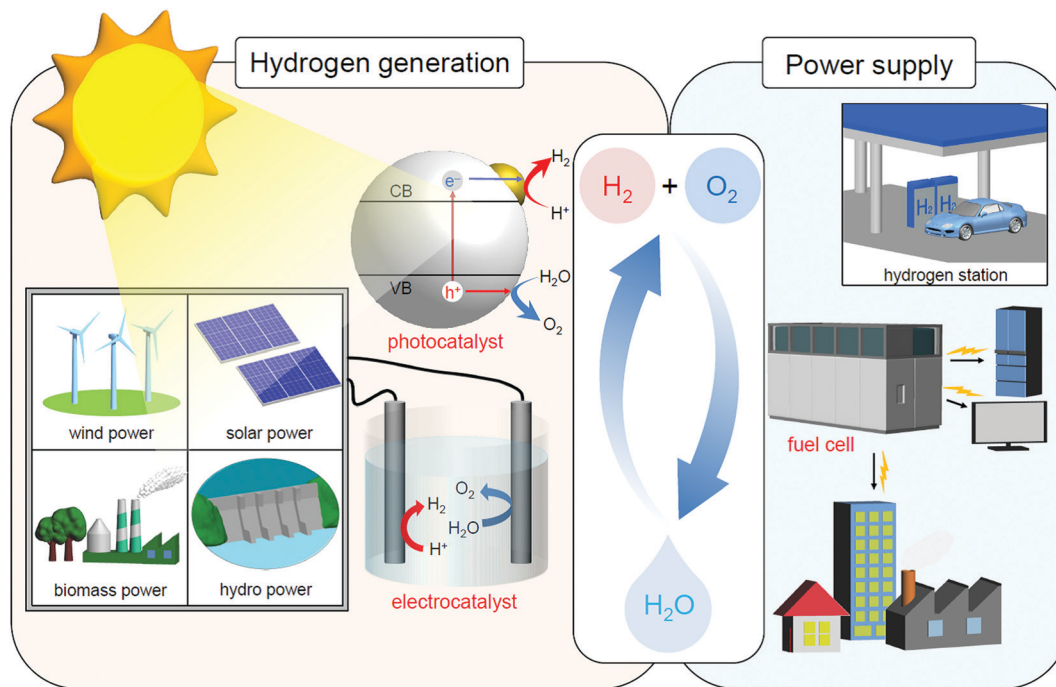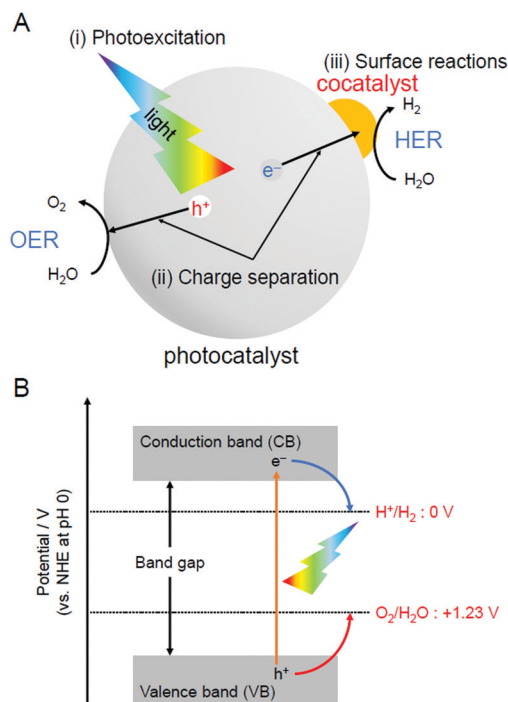
Fig. 1 Schematic of the energy conversion system expected for constructing a sustainable society. Note that sunlight also produces wind, biomass, and hydro power in addition to solar power.

to the surface of the photocatalyst, and (iii) reduction and oxidation of water by excited electrons and holes, respectively (Fig. 2A). Theoretically, when the bottom edge of the CB of the semiconductor photocatalyst is on the negative side of the

Fig. 2 (A) Schematic of photocatalytic reactions: (i) photoexcitation, (ii) charge separation, and (iii) surface reactions. (B) Relationship between the semiconductor band structure and redox potentials of water splitting.

reduction potential of water (0 V $vs.$ normal hydrogen electrode (NHE)), the reduction reaction of water proceeds (Fig. 2B) and H_2 is produced (hydrogen evolution reaction, HER; Fig. 2A). If the top edge of the VB of the semiconductor photocatalyst is on the positive side of the oxidation potential of water (1.23 V $vs.$ NHE), the oxidation reaction of water proceeds (Fig. 2B) and O_2 is generated (oxygen evolution reaction, OER; Fig. 2A). However, even a semiconductor photocatalyst that satisfies these conditions cannot necessarily achieve complete water splitting because of the high activation energy in each reaction. Therefore, to decrease the activation energy of the reaction, metal and/or metal oxide nanoparticles (NPs) made of precious metals are generally loaded on the photocatalyst as active sites (cocatalyst; Fig. 2A).[2,27] This loading of cocatalysts also promotes the separation of electrons and holes in the photocatalyst, thereby suppressing the deactivation of the reaction based on the recombination of electrons and holes. Thus, to enhance the efficiency of the water-splitting reaction, it is extremely effective to improve the cocatalyst in addition to improving the semiconductor photocatalysts.[38]

1.3. Control of cocatalysts

Chemical reactions occurring on the surface of the cocatalyst involve the adsorption and reaction of reactants and desorption of products. Therefore, the efficiency of the chemical reaction is greatly affected by the adsorption/desorption energy of the reactants/products on the surface of the cocatalyst. Previous studies have revealed that the chemical reaction on the surface of the cocatalyst tends to proceed easily when the Gibbs energy in the process of adsorption/desorption of the reactants/products is
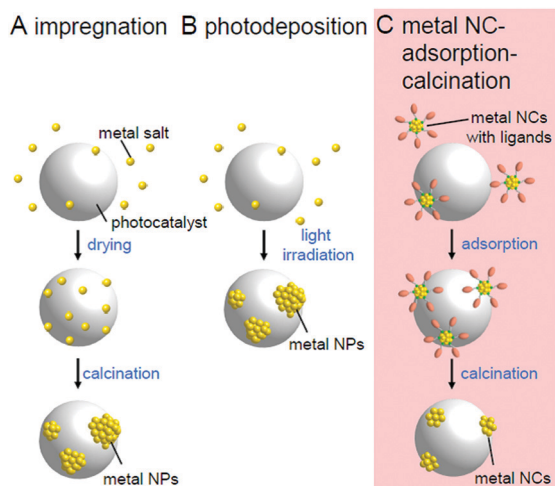
Fig. 3 Comparison of the (A) impregnation, (B) photodeposition, and (C) metal NC adsorption–calcination methods.

moderate. For this reason, metal/metal oxide NPs of group 8–11 elements with sizes of several to several tens of nanometers are generally used as cocatalysts.[2]

In many cases, the cocatalysts are loaded using the impregnation (Fig. 3A)[35] or photodeposition method (Fig. 3B).[40] These methods enable the cocatalyst to be loaded on the photocatalyst using a very simple procedure. When the photodeposition method is used, it is also possible to preferentially load the cocatalyst on the specific crystal planes of the photocatalysts suitable for the reaction.[41] Through studies using these loading methods, it has been clarified that miniaturization of cocatalysts[42] and control of the electronic structure by alloying[43] are extremely effective in creating highly functional water-splitting photocatalysts.

However, the electronic structure of fine metal/metal oxide nanoclusters (NCs) varies greatly depending on the number of constituent atoms and chemical compositions.[44–65] Therefore, if the chemical composition of the fine cocatalysts can be controlled with atomic precision, it is possible to create highly active photocatalysts with the selective loading of a highly active cocatalyst on the surface. In addition, for metal NCs loaded with atomic precision, it is possible to obtain a deep understanding of the electronic/geometrical structures of the cocatalysts and the interaction between the photocatalyst surface and cocatalysts through various high-resolution measurements and theoretical calculations.[66–77] Therefore, the strict control of the cocatalyst is expected to provide deep understanding of the key factors toward high activation. If we would design and create appropriate metal NCs based on the attained information, great enhancement of the water-splitting activities of the photocatalysts could be achieved.[78] Metal NCs can be synthesized with atomic precision using thiolates (SR),[21,79–114] selenolates (SeR),[115–122] phosphines (PR$_3$), alkynes (C≡CR),[123,124] carbon monoxide (CO), dendrimers,[125] *etc.* as protective ligands.[126–143] Furthermore, previous studies have demonstrated that size-controlled metal NCs can be loaded on a support by adsorbing such precise metal NCs

on the support and then removing the protective ligands by calcination (Fig. 3C).[144–146]

1.4. Contents of this review

We aim to improve the functionality of water-splitting photocatalysts to a practical level (Fig. 4) and thereby contribute to the construction of a hydrogen-energy society.[2] To achieve this, we have attempted to strictly control metal NCs on photocatalysts and thereby clarify the details of the effect of controlling the cocatalyst on the water-splitting activity by introducing the precise-control techniques of metal NCs established in the metal NC field into research on water-splitting photocatalysts.[147,148] This feature article summarizes our previous findings.

In Section 2, we first describe the synthesis method and geometrical structure of metal NCs controlled with atomic precision that are used as precursors of cocatalysts. Then, in Section 3, we describe our research on the functionalization of water-splitting photocatalysts using the metal NCs as precursors of cocatalysts. Specifically, the precise loading of the metal NCs on a photocatalyst (Section 3.1), the electronic/geometrical structure of the loaded metal NCs (Section 3.2), the correlation between the types of loaded metal NCs and the water-splitting activity (Section 3.3), and the functionalization of photocatalysts (Section 3.4) are described. After a brief summary in Section 4, the future outlook is described in Section 5.
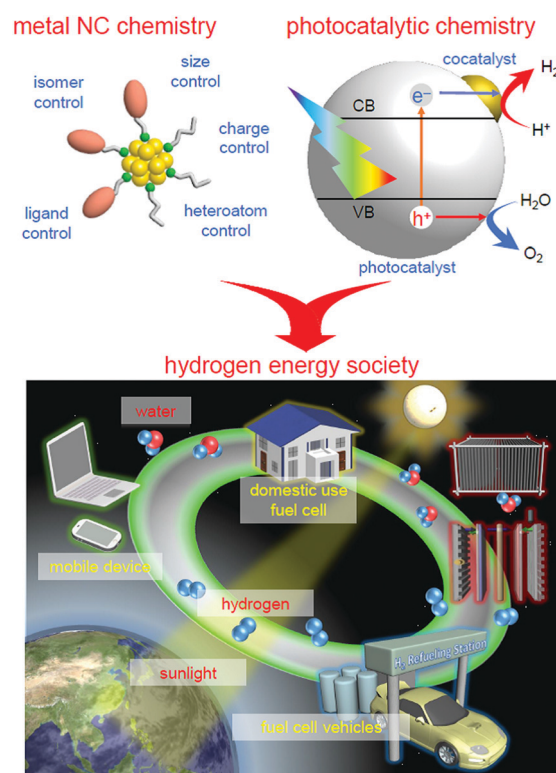

Fig. 4 Schematic of the aims of our study.

2. Ligand-protected atomically precise metal NCs

Since the 1970s, there have been many reports on the precise synthesis of metal NCs using PR_3, CO, and halogens as ligands.[126–143] $[Au_{11}(PPh_3)_7I_3]^+$ (Au = gold; PPh_3 = triphenylphosphine; I = iodine),[149] $Au_{55}(PPh_3)_{12}Cl_6$ (Schmid's Au_{55} cluster; Cl = chlorine),[150] and $[Pt_{3n}(CO)_{6n}]^{2-}$ (Chini cluster; Pt = platinum)[151,152] are representative examples of these metal NCs. However, since 2000, research on metal NCs protected by SR, SeR, and/or C≡CR, which are relatively easily synthesized and can be handled in the atmosphere, has been actively conducted. Herein, we only provide an outline of these metal NCs because several groups including us have already published many reviews on these metal NCs.[72,93,94,153–161]

2.1. Synthesis methods

Fig. 5 presents a typical method for precisely synthesizing SR-protected metal NCs.[93,148] In the method shown in Fig. 5A, metal NCs are prepared by reducing a metal salt or a metal–SR complex with a reducing agent.[162] The metal NCs obtained by this method normally have a distribution in their chemical compositions. Therefore, each metal NC with atomic precision can be obtained by the separation of the mixture using fractionation techniques such as polyacrylamide gel

electrophoresis (PAGE),[79,163–168] high-performance liquid chromatography (HPLC),[55,156,169–182] and thin-layer chromatography (TLC).[183–185] As opposed to separating them, when the mixture is exposed to severe conditions, less stable species transform into stable species, thereby allowing stable metal NCs to be size-selectively synthesized (size focusing; Fig. 5B).[153,186–188] In the method shown in Fig. 5C, metal NCs are grown with relatively uniform size by selecting appropriate experimental conditions for slowly reducing the metal ions and aggregating the obtained metal atoms (slow reduction).[189–192] In the method shown in Fig. 5D, metal NCs with a certain chemical composition are first selectively synthesized, and then the ligands are replaced with ligands with a significantly different structure. This reaction finally results in the selective formation of metal NCs with different chemical compositions (transformation).[193] When using another type of metal salts, metal–SR complexes, or metal NCs as a reactant, it is also possible to selectively synthesize alloy NCs composed of several elements (reconstruction).[194,195] In the method shown in Fig. 5E, after selectively synthesizing metal NCs with a certain chemical composition, the metal NCs are reacted with metal salts,[196] metal–SR complexes,[197] metal NCs,[198] or a metal plate[199] including other types of metal to replace some metal atoms with other metal elements (metal exchange). Under particular reaction conditions, such metal exchange does not occur, and another type of metal atoms or metal ions are deposited on the surface of the metal NCs (deposition of metal atoms/ions; Fig. 5F).[184,200,201] In these synthetic methods, the method shown in Fig. 5A is superior for systematically isolating a series of metal NCs, and the method shown in Fig. 5B–F is superior for size-selectively synthesizing a specific metal NC. In addition to these methods, there have been several reports on the synthesis of new metal NCs using a combination of several of the methods shown in Fig. 5.[202]
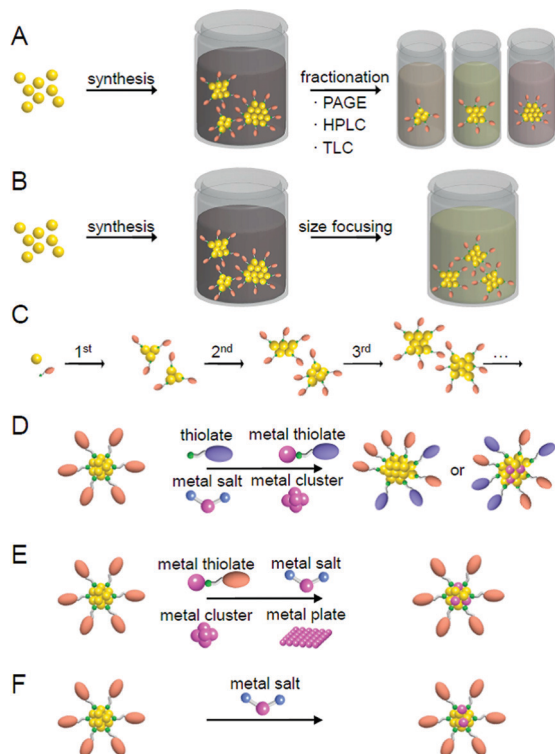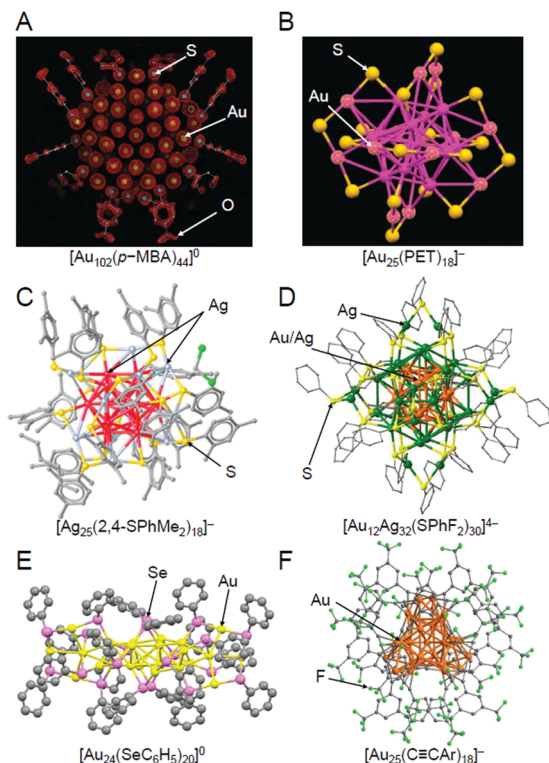

Fig. 5 Typical methods for the precise synthesis of metal clusters: (A) fractionation, (B) size focusing, (C) slow reduction, (D) transformation/reconstruction, (E) metal exchange, and (F) deposition of metal atoms/ions.

2.2. Geometrical structures

When research on SR-protected metal NCs began, they were thought to have a geometrical structure where the metal core is covered by SR.[203] However, the density functional theory (DFT) calculations on $[Au_{38}(SCH_3)_{24}]^0$ by Häkkinen et al. in 2006[204] suggested that SR-protected metal NCs have a geometrical structure where the metal core is covered by Au–SR oligomers (now called staples). In the next year, this "divide and protect" structure was experimentally verified by Kornberg et al. through single-crystal X-ray diffraction (SC-XRD) analysis of $[Au_{102}(p\text{-}MBA)_{44}]^0$ (p-MBA = p-mercaptobenzoic acid) (Fig. 6A).[111,205] Since then, the geometrical structures of many SR-protected metal NCs have been determined by SC-XRD,[153,154] and almost all of the SR-protected metal NCs have been observed to have such "divide and protect" structures (Fig. 6B–D). Several research groups, including those of Zhu, Wang, Jiang, Tsukuda, and Pei et al., have shown that SeR-protected metal NCs (Fig. 6E)[206,207] and C≡CR-protected metal NCs (Fig. 6F)[124,208,209] also have such "divide and protect" framework structures.

Fig. 6 Geometric structures of (A) $[Au_{102}(p\text{-}MBA)_{44}]^0$,[111] (B) $[Au_{25}(PET)_{18}]^-$ (PET = phenylethanethiolate),[112] (C) $[Ag_{25}(2,4\text{-}SPhMe_2)_{18}]^-$ (2,4-SPhMe_2 = 2,4-dimethylbenzenethiolate),[113] (D) $[Au_{12}Ag_{32}(SPhF_2)_{30}]^{4-}$ (SPhF_2 = 3,4-difluorothiophenol),[114] (E) $[Au_{24}(SeC_6H_5)_{20}]^0$ (SeC_6H_5 = benzeneselenolate),[206] and (F) $[Au_{25}(C{\equiv}CAr)_{18}]^-$ (C≡CAr = 3,5-bis(trifluoromethyl)phenylethynyl).[124] The gray points represent carbon atoms. Hydrogen atoms are not shown. $Au_{25}(SG)_{18}$, which was used in our study, has been considered to have a similar framework structure to $[Au_{25}(PET)_{18}]^-$ (B), although its geometric structure has not been determined by SC-XRD to date. Reproduced with permission from ref. 111, 112, 113, 114, 206 and 124. Copyright 2007 American Association for the Advancement of Science, Copyright 2008 American Chemical Society, Copyright 2015 American Chemical Society, Copyright 2013 Springer Nature Communications, Copyright 2014 American Chemical Society, and Copyright 2019 Wiley-VCH, respectively.

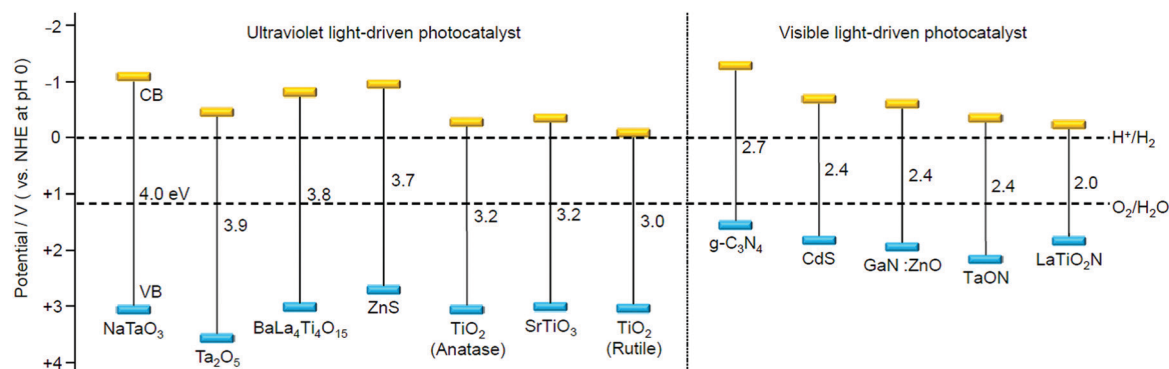# 3. Activation of water-splitting photocatalysts using atomically precise metal NCs

We aim to functionalize water-splitting photocatalysts that can be used as practical materials. Therefore, we used some of the most advanced photocatalysts. Fig. 7 shows the band structures of several advanced photocatalysts.[28,29,210,211] Among them, $BaLa_4Ti_4O_{15}$ (Fig. 8A)[210] or $SrTiO_3$ (Fig. 8B)[212,213] were used in our research. $BaLa_4Ti_4O_{15}$ is a photocatalyst[210] developed by Kudo *et al.* in 2009 and has a perovskite structure (Fig. 8A) (band gap = 3.8 eV). Because this photocatalyst is not commercially available, $BaLa_4Ti_4O_{15}$ was synthesized in our laboratory using a previously reported procedure. $SrTiO_3$ also has a perovskite structure with a band gap of 3.2 eV (Fig. 8B). The band gap of this photocatalyst can be tuned by doping with different elements (rhodium (Rh), lanthanum (La), *etc.*) and the obtained $SrTiO_3$ doped with different elements ($SrTiO_3$:Rh, $SrTiO_3$:La, Rh, *etc.*) has been used as a photocatalyst for H_2 evolution in Z-scheme systems.[26,31,214–217] Because $SrTiO_3$ is already on the market, we used a commercial product for this photocatalyst.

3.1. Loading of atomically precise metal NCs on photocatalysts

When a metal oxide is added to water, hydroxyl groups (–OH) are normally formed on the surface. Hydrophilic metal NCs with proton functional groups are easily adsorbed on such surfaces.[146,218–222] Therefore, we first worked on loading metal NCs on $BaLa_4Ti_4O_{15}$ using hydrophilic metal NCs as precursors.

3.1.1. Use of hydrophilic Au NCs as a precursor

Loading of Au_{25}. In our first effort, we used glutathionate (SG)-protected Au_{25} NCs ($Au_{25}(SG)_{18}$; Fig. 6B) as a precursor, which are stable in solution and can be size-selectively synthesized.[79,187,223,224] In this experiment, $Au_{25}(SG)_{18}$ was first adsorbed on $BaLa_4Ti_4O_{15}$ by stirring them in water ($Au_{25}(SG)_{18}/BaLa_4Ti_4O_{15}$).[225] In the optical absorption spectrum of the aqueous solution after adsorption, optical absorption was hardly observed, indicating that almost all of the $Au_{25}(SG)_{18}$ was adsorbed on $BaLa_4Ti_4O_{15}$. Glutathionate has two carboxyl groups and one amino

Fig. 7 Energy-band diagram of several water-splitting photocatalysts and the redox potential of the hydrogen- and oxygen-evolution reations.[28,29,210,211]
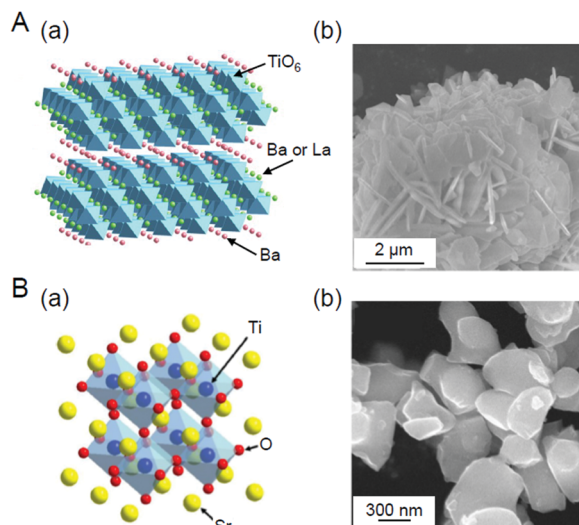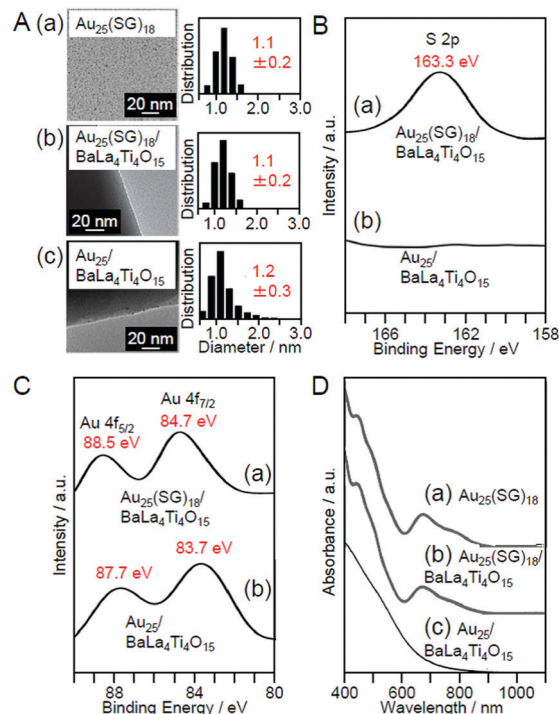
Fig. 8 (A) (a) Geometric structure of BaLa$_4$Ti$_4$O$_{15}$[247] and (b) scanning electron microscope (SEM) image of the prepared BaLa$_4$Ti$_4$O$_{15}$.[270] (B) (a) Geometric structure of SrTiO$_3$ and (b) SEM image of the prepared SrTiO$_3$.[231] Reproduced with permission from ref. 247 and 270. Copyright 2018 American Chemical Society, Copyright 2020 Wiley-VCH.

Fig. 9 (A) TEM images and size distributions of (a) Au$_{25}$(SG)$_{18}$, (b) Au$_{25}$(SG)$_{18}$/BaLa$_4$Ti$_4$O$_{15}$, and (c) Au$_{25}$/BaLa$_4$Ti$_4$O$_{15}$ (0.1 wt% Au). (B) S 2p XPS spectra and (C) Au 4f XPS spectra of (a) Au$_{25}$(SG)$_{18}$/BaLa$_4$Ti$_4$O$_{15}$ and (b) Au$_{25}$/BaLa$_4$Ti$_4$O$_{15}$. (D) (a) Optical absorption spectra of Au$_{25}$(SG)$_{18}$ aqueous solution and the diffuse reflectance spectrum of (b) Au$_{25}$(SG)$_{18}$/BaLa$_4$Ti$_4$O$_{15}$ and (c) Au$_{25}$/BaLa$_4$Ti$_4$O$_{15}$. Reproduced with permission from ref. 225. Copyright 2013 Royal Society of Chemistry.

group.[226] It can be considered that Au$_{25}$(SG)$_{18}$ was efficiently adsorbed on the photocatalyst because the polar functional groups of Au$_{25}$(SG)$_{18}$ formed hydrogen bonds with the –OH groups on the surface of BaLa$_4$Ti$_4$O$_{15}$.

Then, the obtained Au$_{25}$(SG)$_{18}$/BaLa$_4$Ti$_4$O$_{15}$ was calcined in an electric furnace. Thermogravimetric analysis (TGA) of Au$_{25}$(SG)$_{18}$/BaLa$_4$Ti$_4$O$_{15}$ showed that most of the SG can be removed at 300 °C.[225] Thus, Au$_{25}$(SG)$_{18}$/BaLa$_4$Ti$_4$O$_{15}$ was calcined at 300 °C for 2 h under reduced pressure. Fig. 9A–D present the transmission electron microscope (TEM) images, S 2p and Au 4f spectra obtained by X-ray photoelectron spectroscopy (XPS), and optical adsorption/diffuse reflectance spectrum of the photocatalysts before and after calcination (Au$_{25}$(SG)$_{18}$/BaLa$_4$Ti$_4$O$_{15}$ and Au$_{25}$/BaLa$_4$Ti$_4$O$_{15}$), respectively, for the photocatalysts containing Au with a weight ratio of 0.1 wt% (0.1 wt% Au). In the TEM image of the sample after calcination (Fig. 9A(c)), only particles with sizes similar to those before calcination were observed, indicating that calcination did not cause the aggregation of NCs. In the S 2p spectrum (Fig. 9B(b)), a peak was hardly observed, indicating that most of the ligands were removed by calcination. In the Au 4f spectrum of the sample after calcination, the peak positions (83.7 and 87.7 eV; Fig. 9C(b)) were different from those of the sample before calcination (84.7 and 88.5 eV; Fig. 9C(a)) and were located at an energy near those expected for Au(0) (84.0 and 87.7 eV). For Au$_{25}$(SG)$_{18}$, the Au 4f peaks appear on the oxidation side (high-energy side) compared with Au(0) because of the partial charge transfer from Au to S.[225] The shift of the Au 4f peaks after calcination strongly indicates that the ligands were removed by calcination and therefore that Au in the metallic state was loaded on BaLa$_4$Ti$_4$O$_{15}$. In the diffuse reflectance spectrum of the photocatalyst after calcination (Fig. 9D(c)), the peaks in the visible region, which are characteristic of

Au$_{25}$(SG)$_{18}$, were not observed. In the optical absorption spectrum of Au$_{25}$(SR)$_{18}$ (Fig. 9D(a)), the peaks in the region of 600–800 nm are attributed to the absorption originating in the central Au$_{13}$ core of Au$_{25}$(SR)$_{18}$ (Fig. 6B).[112,227–230] It can be interpreted that these peaks disappeared because the ligands were removed by calcination, thereby resulting in a drastic change of the structure of the NCs. The slight increase in the particle size of the photocatalysts after calcination (Fig. 9A) can also be explained by this structural change. These results confirmed that the ligands were removed from Au$_{25}$(SG)$_{18}$/BaLa$_4$Ti$_4$O$_{15}$ by calcination while maintaining the particle size of the Au$_{25}$ NC (Au$_{25}$/BaLa$_4$Ti$_4$O$_{15}$).[225] In our later research, it became clear that the precise loading of Au$_{25}$ using Au$_{25}$(SG)$_{18}$ as a precursor can also be performed in the same way when SrTiO$_3$ is used as a photocatalyst.[231]

Effect of the types of precursor NCs. We also attempted to load Au$_n$ NCs (n represents the number of Au atoms) composed of other numbers of constituent atoms on BaLa$_4$Ti$_4$O$_{15}$. In this experiment, Au$_n$(SG)$_m$ NCs (n = 10, 15, 18, 22, 25, 29, 33, or 39; m represents the number of ligands[79]) were used as a precursor. First, an aqueous solution containing Au$_n$(SG)$_m$ NCs (0.1 wt% Au) and BaLa$_4$Ti$_4$O$_{15}$ was stirred at room temperature for 1 h. Then, the adsorption efficiency of the Au$_n$(SG)$_m$ NCs was estimated by evaluating the amount of Au contained in the supernatant solution after stirring using inductively coupled

plasma-mass spectrometry. The results indicated that the $Au_n(SG)_m$ NCs adsorbed on the photocatalyst with adsorption efficiencies of 98.8% ($n = 10$), 97.8% ($n = 15$), 96.6% ($n = 18$), 99.1% ($n = 22$), 99.2% ($n = 25$), 97.9% ($n = 29$), 96.7% ($n = 33$), and 99.4% ($n = 39$), respectively.[232] These results indicate that $Au_n(SG)_m$ NCs with 0.1 wt% Au can be adsorbed on $BaLa_4Ti_4O_{15}$

at high adsorption efficiencies regardless of the chemical compositions. However, these results also imply that $Au_n(SG)_m$ NCs cannot necessarily be adsorbed on $BaLa_4Ti_4O_{15}$ with an adsorption efficiency of 100%. The adsorption efficiencies did not exceed the above values even when the stirring time was extended to 2 h. Thus, the results indicate that a chemical
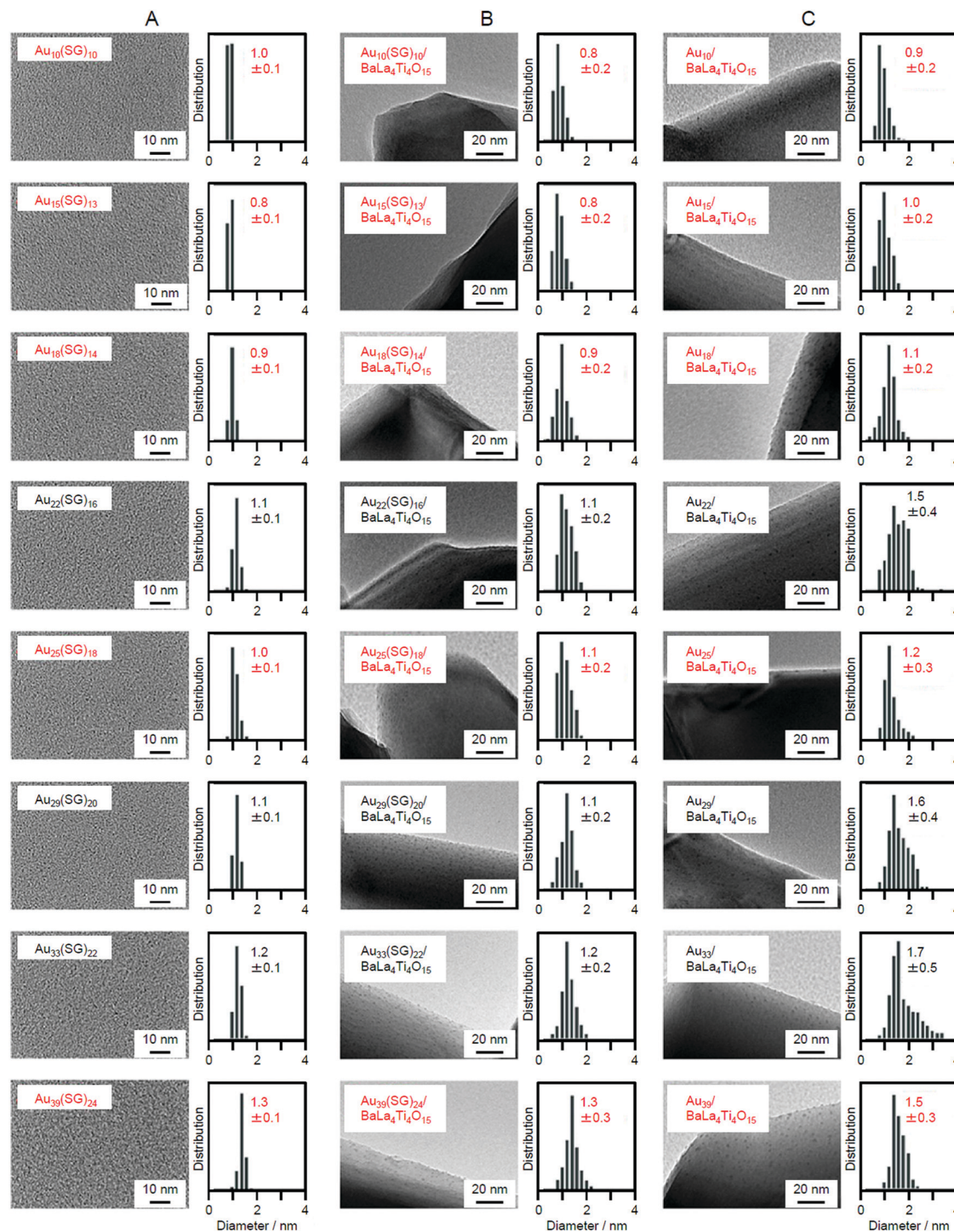

Fig. 10 TEM images and size distributions of the different (A) $Au_n(SG)_m$ NCs, (B) $Au_n(SG)_m/BaLa_4Ti_4O_{15}$, and (C) $Au_n/BaLa_4Ti_4O_{15}$ (0.1 wt% Au). The Au_n NCs highlighted in red maintained their particle size during a series of loading processes. Reproduced with permission from ref. 232. Copyright 2015 American Chemical Society.

equilibrium was achieved between the aqueous solution of the $Au_n(SG)_m$ NCs and $Au_{25}(SG)_{18}/BaLa_4Ti_4O_{15}$ at the above adsorption efficiencies. These results warn that the actual amount of $Au_n(SG)_m$ NCs adsorbed on $BaLa_4Ti_4O_{15}$ cannot be accurately estimated solely from the mixing ratio of $Au_n(SG)_m$ NCs and $BaLa_4Ti_4O_{15}$.

Fig. 10A–C present TEM images and the size distributions of the $Au_n(SG)_m$ NCs, $Au_n(SG)_m/BaLa_4Ti_4O_{15}$, and $Au_n/BaLa_4Ti_4O_{15}$, respectively. For all the $Au_n(SG)_m$ NCs, the average particle sizes and particle-size distributions were relatively similar for the $Au_n(SG)_m$ NCs and $Au_n(SG)_m/BaLa_4Ti_4O_{15}$ (Fig. 10A and B).[232] This finding indicates that no significant change in the particle size (especially the increase of the particle size) of the $Au_n(SG)_m$ NCs occurs between before and after adsorption. In contrast, different behaviors were observed for $Au_n/BaLa_4Ti_4O_{15}$ depending on the type of $Au_n(SG)_m$ NCs. According to Fig. 10, the NCs can be broadly classified into the following two groups based on their similar phenomena: (1) n = 10, 15, 18, 25, and 39 and (2) n = 22, 29, and 33. The Au_n NCs in group 1 maintained a narrow distribution of their particle sizes even after calcination, although the average particle size slightly increased during calcination (Fig. 10B and C). In contrast, for the Au_n NCs in group 2, the average particle size significantly increased during calcination. These two groups are in good agreement with the classification of the stability of $Au_n(SG)_m$ NCs against dissociation in aqueous solution: the $Au_n(SG)_m$ NCs in group 2 dissociate in aqueous solution (release of SG or an Au–SR complex) more quickly than those in group 1.[79] From these results, it can be considered that the stability of $Au_n(SG)_m$ NCs against dissociation is greatly related to the increase in the particle size of the Au_n NCs in group 2. Most likely, part of the $Au_n(SG)_m$ NCs was dissociated during the stirring process, and the Au–SG complex produced by such dissociation was adsorbed on $BaLa_4Ti_4O_{15}$ together with the $Au_n(SG)_m$ NCs. It is presumed that the observed phenomenon occurred because such an Au–SG complex promoted the aggregation of Au_n NCs on $BaLa_4Ti_4O_{15}$ during calcination. These results demonstrate that using Au_n NCs with high stability in solution as a precursor is essential to precisely load the Au_n NCs on $BaLa_4Ti_4O_{15}$ (Fig. 11).

Effect of loading amounts. We also investigated the effect of the amount of adsorbed NCs on the particle size of the loaded
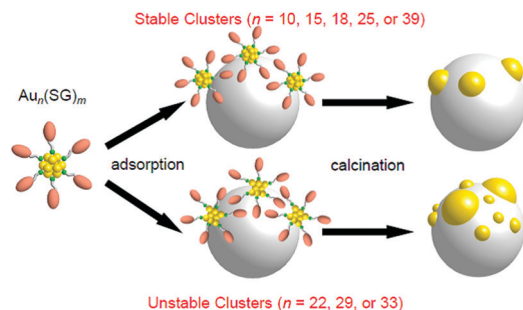

Fig. 11 Schematic of the aggregation of $Au_n(SG)_m$ on the photocatalyst depending on the cluster size (0.1 wt% Au). Reproduced with permission from ref. 232. Copyright 2015 American Chemical Society.
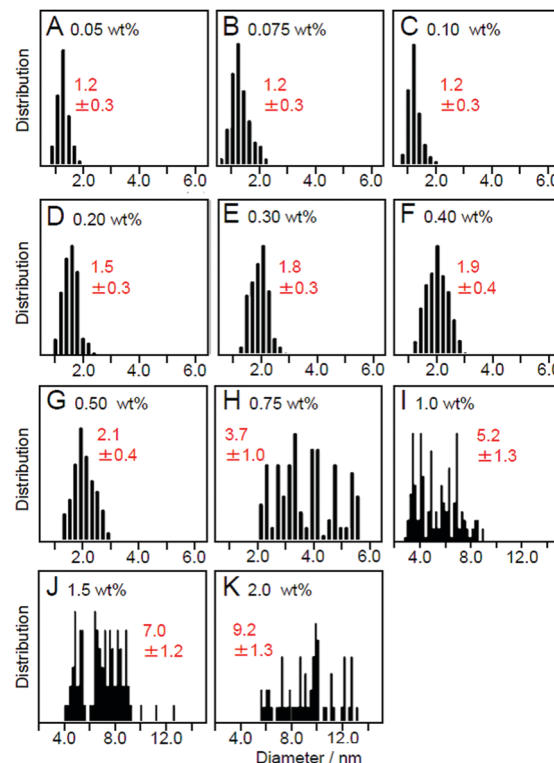

Fig. 12 Size distributions of Au NPs estimated from TEM images of $Au_{25}/BaLa_4Ti_4O_{15}$ containing (A) 0.05 wt%, (B) 0.075 wt%, (C) 0.10 wt%, (D) 0.20 wt%, (E) 0.30 wt%, (F) 0.40 wt%, (G) 0.50 wt%, (H) 0.75 wt%, (I) 1.0 wt%, (J) 1.5 wt%, and (K) 2.0 wt% Au. Reproduced with permission from ref. 225. Copyright 2013 Royal Society of Chemistry.

NCs using $Au_{25}(SG)_{18}$ as a precursor. Fig. 12 lists the particle size distributions of the loaded particles, which were estimated from TEM images of photocatalysts containing each amount of $Au_{25}(SG)_{18}$. When the amount of adsorption of $Au_{25}(SG)_{18}$ was higher than 0.2 wt% Au, the particle size of the loaded Au NCs increased during calcination.[225] Under these conditions, $Au_{25}(SG)_{18}$ should be adsorbed on $BaLa_4Ti_4O_{15}$ at a narrow distance. This appears to induce the aggregation of $Au_{25}(SG)_{18}$ in the calcination process, leading to the increase of the particle sizes. These results indicate that the loaded amount must be less than 0.2 wt% Au to load Au_{25} NCs on the photocatalyst while maintaining the particle size of the precursor NCs. The maximum water-splitting activity of the resulting photocatalysts was observed when the amount of loaded Au was 0.1 wt%, and the water-splitting activity decreased when it was greater than 0.2 wt% Au.[225] The following two factors are considered to be involved in this phenomenon: (1) a decrease in the proportion of surface Au atoms in the cocatalyst with an increase in particle size and (2) a decrease in the amount of light absorption of the photocatalyst with an increase in the amount of cocatalyst. Based on these results, the amount of loaded cocatalyst was fixed to 0.1 wt% Au in the subsequent studies using Au_n NCs and their related alloy NCs as cocatalysts.

3.1.2. Use of hydrophobic Au NCs as a precursor. As described above, when hydrophilic Au_n NCs are used as

the precursor, the Au_n NCs can be easily loaded on the photocatalyst. However, hydrophobic metal NCs easily form crystals; thus, it is possible to determine their geometric structure using SC-XRD.[153,154] Thus, most of the metal NCs synthesized to date have been hydrophobic metal NCs. Therefore, we also attempted to establish a method for loading hydrophobic metal NCs on the photocatalyst at high efficiency.[233] Specifically, we replaced part of the hydrophobic ligands with hydrophilic ligands (ligand exchange; Fig. 13A).
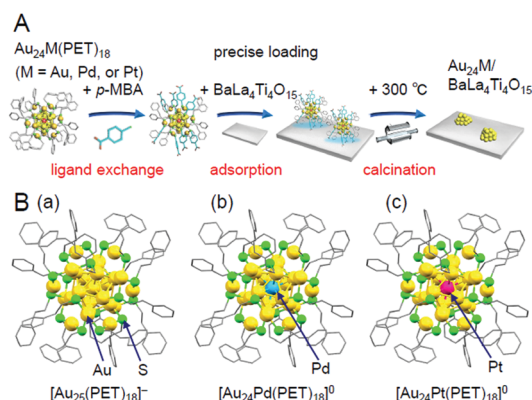
In this experiment, phenylethanethiolate (PET), which has often been used as a hydrophobic ligand, was used as the ligand. First, $Au_{25}(PET)_{18}$ (Fig. 13B(a)),[112] $Au_{24}Pd(PET)_{18}$ (Pd = palladium; Fig. 13B(b)),[96] and $Au_{24}Pt(PET)_{18}$ (Fig. 13B(c))[96] were synthesized with atomic precision. Then, some of the PET was replaced with hydrophilic p-MBA[111] by a ligand-exchange reaction. The matrix-assisted laser desorption/ionization (MALDI) mass spectra obtained for the sample after ligand exchange only contained peaks attributable to $Au_{25}(PET)_{18-y}(p\text{-MBA})_y$ (y = 7–14; Fig. 14A), $Au_{24}Pd(PET)_{18-y}(p\text{-MBA})_y$ (y = 1–9; Fig. 14B), and $Au_{24}Pt(PET)_{18-y}(p\text{-MBA})_y$ (y = 3–10; Fig. 14C). No intrinsic changes were observed in the diffuse reflectance spectra of the NCs or the TEM images before and after ligand exchange. These results indicate that some of the ligands were replaced in each NC without any change in the framework structure of the NC. Each NC was adsorbed on $BaLa_4Ti_4O_{15}$ at a high adsorption efficiency of >96% after the ligand exchange (Fig. 14D–F). In the Au L_3-edge Fourier-transform extended X-ray absorption fine structure (FT-EXAFS) spectra of the photocatalysts after calcination, almost no peaks attributed to the Au–S bond (∼1.8 Å) were observed (Fig. 14G). The coordination numbers of Au (7.1–7.7) of each of the loaded NCs estimated

from the Au L_3-edge FT-EXAFS spectra were between those expected for cuboctahedral-structured Au_{13} (5.5) and Au_{55} (7.9). In the TEM images of the photocatalysts after calcination, particles with sizes similar to those before calcination were observed. These results confirmed that the ligands were removed from $Au_{25}(PET)_{18-y}(p\text{-MBA})_y$, $Au_{24}Pd(PET)_{18-y}(p\text{-MBA})_y$, and $Au_{24}Pt(PET)_{18-y}(p\text{-MBA})_y$ by calcination and, therefore, bare Au_{25}, $Au_{24}Pd$, and $Au_{24}Pt$ were loaded on $BaLa_4Ti_4O_{15}$ without any aggregation.[233]

3.2. Electronic and geometric structures of loaded metal NCs

3.2.1. Electronic structures. Au_n NCs (n = 10, 15, 18, 25, and 39), $Au_{24}Pd$, or $Au_{24}Pt$ loaded-$BaLa_4Ti_4O_{15}$ ($Au_n/BaLa_4Ti_4O_{15}$, $Au_{24}Pd/BaLa_4Ti_4O_{15}$, and $Au_{24}Pt/BaLa_4Ti_4O_{15}$) exhibited optical absorption different from those with ligands. This finding indicates that the electronic structures of the loaded metal NCs differed from those of the precursor metal NCs. As later described in Section 3.2.2, the calcination process significantly changed the geometric structure of the metal NCs. The change of the electronic structure of the metal NCs is considered to be mainly caused by the change in the framework structure. The Au L_3-edge X-ray absorption near-edge structure (XANES) spectra (Fig. 15) showed that the electron density of the Au 5d orbitals in $Au_{25}/BaLa_4Ti_4O_{15}$ is higher than that of Au foil. This result indicates that Au is reduced in $Au_{25}/BaLa_4Ti_4O_{15}$, suggesting that partial charge transfer occurs from $BaLa_4Ti_4O_{15}$ to Au_{25} in $Au_{25}/BaLa_4Ti_4O_{15}$. Au L_3-edge XANES analysis revealed that substituting Au in $Au_{25}/BaLa_4Ti_4O_{15}$ with Pd or Pt further increases the electron density of Au (Fig. 15). This result implies that partial charge transfer occurs from Pd (electronegativity = 2.20) to Au (electronegativity = 2.54) and Pt (electronegativity = 2.28) to Au in $Au_{24}Pd$ and $Au_{24}Pt$, respectively, due to the difference in the electronegativity of the two elements.

3.2.2. Geometric structures. For $Au_{25}/BaLa_4Ti_4O_{15}$, $Au_{24}Pd/BaLa_4Ti_4O_{15}$, and $Au_{24}Pt/BaLa_4Ti_4O_{15}$, the geometric structure of the loaded clusters was also investigated (Fig. 16).[233]
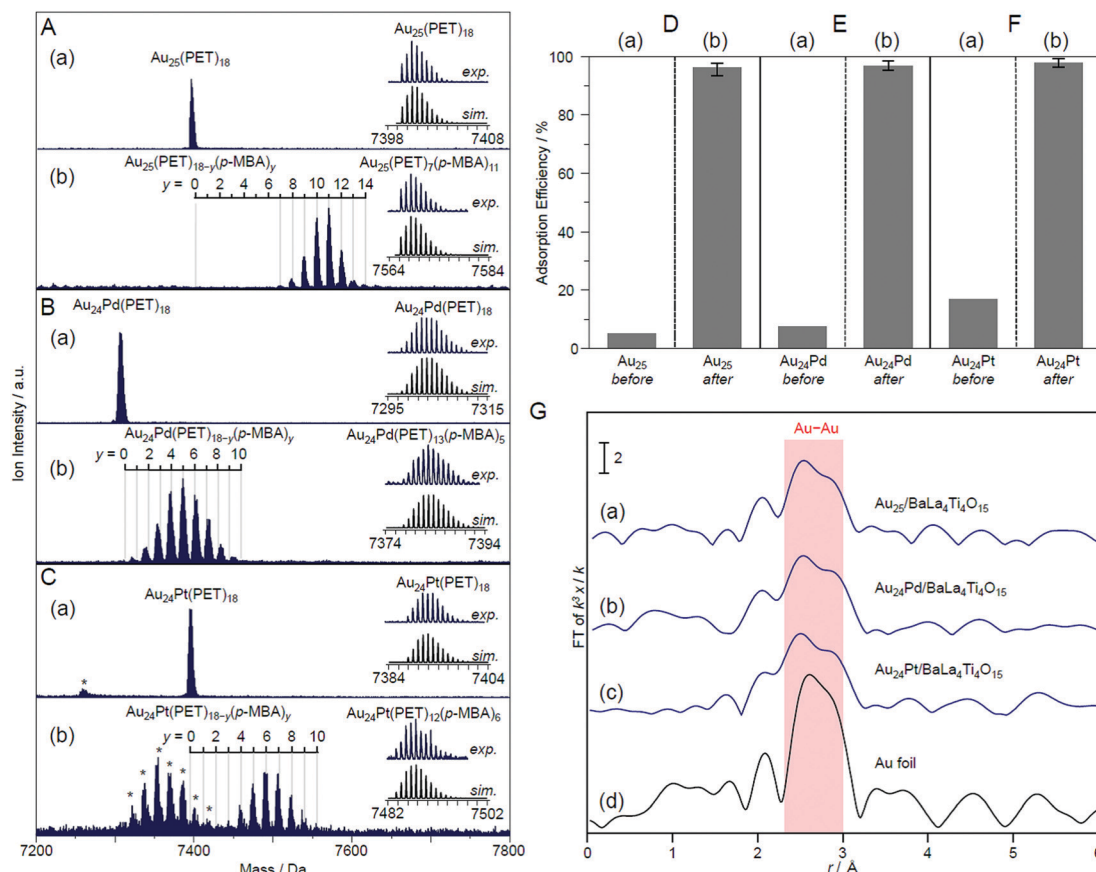
Framework structure of $Au_{24}M$ (M = Au, Pd, or Pt). Experiments and DFT calculations by other groups have shown that fine isolated Au_n clusters tend to have a planar geometry.[234–239] In addition, DFT calculations on Au_{10}/metal oxide predicted that Au_{10} is most stable on metal oxides when they have a two-dimensional structure.[240] Based on these results, Au_{25} is presumed to have a relatively planar geometry on $BaLa_4Ti_4O_{15}$ (Fig. 16A). Indeed, the coordination number of Au estimated from the Au L_3-edge FT-EXAFS and the particle size observed in TEM and high-resolution (HR)-TEM images of $Au_{25}/BaLa_4Ti_4O_{15}$ strongly support this interpretation.[233]

On the other hand, Au L_3-edge FT-EXAFS, TEM, and HR-TEM measurements suggest that alloy NCs (especially $Au_{24}Pt$ NCs) have a more three-dimensional structure than Au_{25} NCs.[233] For bare Au_n NCs produced in the gas phase, it has been shown that doping with Pd or Pt induces the formation of a three-dimensional structure in a smaller size region than for pure Au_n.[241,242] $Au_{24}Pd$ and $Au_{24}Pt$ can be considered to have a more

Fig. 13 (A) Schematic of the preparation procedure for $Au_{24}M/BaLa_4Ti_4O_{15}$ (M = Au, Pd, or Pt) using hydrophobic metal NCs as a precursor.[233] (B) Geometric structures of (a) $[Au_{25}(PET)_{18}]^-$,[112] (b) $[Au_{24}Pd(PET)_{18}]^0$,[96] and (c) $[Au_{24}Pt(PET)_{18}]^0$.[96] These metal NCs have been revealed to have a geometric structure where the $Au_{12}M$ metal core (M = Au, Pd, or Pt) is surrounded by six –PET–[Au–PET–]$_2$ staples.[96,112] In $[Au_{24}Pd(PET)_{18}]^0$ and $[Au_{24}Pt(PET)_{18}]^0$, both Pd and Pt are located at the central position of the $Au_{12}M$ metal core. Reproduced from ref. 233, 112 and 96. Copyright 2019 American Chemical Society, Copyright 2016 Royal Society of Chemistry, and Copyright 2008 American Chemical Society, respectively.

Fig. 14 Negative-ion MALDI mass spectra of (a) $Au_{24}M(PET)_{18}$ and (b) $Au_{24}M(PET)_{18-y}(p\text{-}MBA)_y$ for M = (A) Au, (B) Pd, and (C) Pt. The experimental and simulated isotope patterns are compared in the inserts. In these spectra, the asterisks indicate the laser fragments. Adsorption efficiency of $Au_{24}M(SR)_{18}$ for M = (D) Au, (E) Pd, and (F) Pt (SR = PET or p-MBA) on $BaLa_4Ti_4O_{15}$ (a) before and (b) after the ligand-exchange reaction. (G) Au L_3-edge FT-EXAFS spectra of $Au_{24}M/BaLa_4Ti_4O_{15}$ for M = (a) Au, (b) Pd, and (c) Pt together with that of (d) Au foil. Reproduced with permission from ref. 233. Copyright 2019 American Chemical Society.
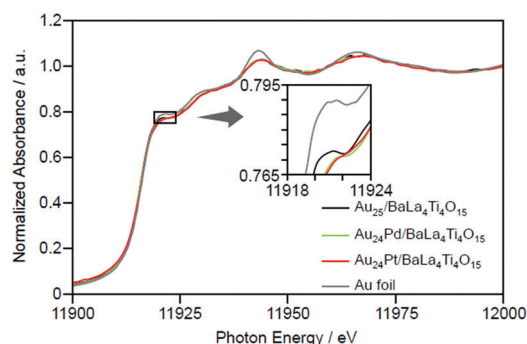
Fig. 15 Au L_3-edge XANES spectra of $Au_{24}M/BaLa_4Ti_4O_{15}$ (M = Au, Pd, and Pt) together with that of Au foil. Reproduced with permission from ref. 233. Copyright 2019 American Chemical Society.

steric structure than Au_{25} because a similar heteroatom substitution effect is induced in $Au_{24}Pd/BaLa_4Ti_4O_{15}$ and $Au_{24}Pt/BaLa_4Ti_4O_{15}$ (Fig. 16B and C).

Substitution position of heteroatoms in $Au_{24}M/BaLa_4Ti_4O_{15}$ (M = Pd or Pt). For $Au_{24}Pd/BaLa_4Ti_4O_{15}$, the EXAFS results
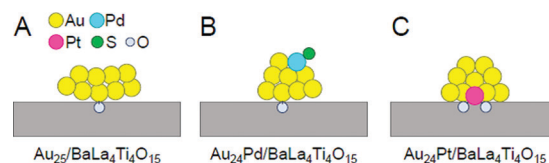
Fig. 16 Proposed structures of $Au_{24}M/BaLa_4Ti_4O_{15}$ for M = (A) Au, (B) Pd, and (C) Pt. Reproduced with permission from ref. 233. Copyright 2019 American Chemical Society.

indicate that Pd is located on the surface of the loaded metal NCs and is bound to S (Fig. 16B).[233] In the precursor $Au_{24}Pd(SR)_{18}$, Pd was located at the center of the metal core and was not bound to S (Fig. 13B(b)). Therefore, it is inferred that this geometric structure was formed because Pd moved to the surface of the particles during calcination and combined with S that was separated from Au. On the other hand, Pt was found to be located at the interface between $Au_{24}Pt$ and $BaLa_4Ti_4O_{15}$ and bound to several O in $BaLa_4Ti_4O_{15}$ (Fig. 16C).[233]

Pt forms a stronger bond with O than Au (318.4 ± 6.7 kJ mol^{-1} for Pt–O vs. 223 ± 21.1 kJ mol^{-1} for Au–O)[243] and can bind with multiple O, thereby causing Pt to be located at the interface

between $Au_{24}Pt$ NCs and $BaLa_4Ti_4O_{15}$ (Fig. 16C). On the other hand, Pd forms a weaker bond with O than Au (145 ± 11.1 kJ mol^{-1} for Pd–O $vs.$ 223 ± 21.1 kJ mol^{-1} for Au–O).[243] Thus, it is thermodynamically undesirable for Pd to be located at the interface. Because Pd has a higher surface energy than Au (2.003 J m^{-2} for the Pd (111) surface $vs.$ 1.506 J m^{-2} for the Au (111) surface),[244] it is also thermodynamically undesirable for Pd to be located on the surface. Accordingly, the Pd–S bond appears to be formed to suppress the instability of the NCs (Fig. 16B).

Immobilization of metal NCs at the interface in Au$_{24}$M/BaLa$_4$-Ti$_4$O$_{15}$ (M = Au, Pd, or Pt). As mentioned above, Au was located at the interface in $Au_{25}/BaLa_4Ti_4O_{15}$ and $Au_{24}Pd/BaLa_4Ti_4O_{15}$. The binding energy of Au and O is not very high. Moreover, for Au_{10}/metal oxide, DFT calculations predicted that planar Au_{10} forms an Au–O bond with the metal-oxide surface at a single point.[240] In the Au L$_3$-edge FT-EXAFS spectra of $Au_{25}/BaLa_4Ti_4O_{15}$ and $Au_{24}Pd/BaLa_4Ti_4O_{15}$, no strong peaks attributed to Au–O were observed.[233] Thus, it appears that there are only a small number of Au–O bonds in $Au_{25}/BaLa_4Ti_4O_{15}$ and $Au_{24}Pd/BaLa_4Ti_4O_{15}$, and thus the metal NCs are weakly immobilized on $BaLa_4Ti_4O_{15}$ in these photocatalysts (Fig. 16A and B).

On the other hand, in $Au_{24}Pt/BaLa_4Ti_4O_{15}$, Pt was located at the interface and formed multiple Pt–O bonds with $BaLa_4Ti_4O_{15}$ (Fig. 16C). Pt can bind more strongly with O than Au. Thus, $Au_{24}Pt$ is considered to be more strongly immobilized on $BaLa_4Ti_4O_{15}$ than Au_{25} and $Au_{24}Pd$. In fact, $Au_{24}Pt$ did not aggregate on $BaLa_4Ti_4O_{15}$ as much as Au_{25} and $Au_{24}Pd$ during the water-splitting reaction.[233] This fact also strongly supports our above interpretation.

3.3. Effect of controlling the cocatalysts on the catalytic activity

The effect of the chemical composition of the cocatalyst on the water-splitting activity was successfully elucidated by controlling the chemical composition of the metal NCs with atomic precision.

3.3.1. Effect of the Au NC size. The water-splitting reaction was performed by dispersing 500 mg of photocatalyst in 350 mL of water and irradiating it with ultraviolet light from inside using a high-pressure mercury lamp (400 W). The amount of evolved gas was quantified by gas chromatography (Fig. 17). When the gas accumulates in the reaction cell, the gas evolution is suppressed, and thus the changes in gas evolution over time cannot be accurately tracked.[245] Hence, the gas was flowed through the reaction cell in our studies (Fig. 17).

Under conditions of flowing CO$_2$. In our early studies,[225,232] CO$_2$ was flowed into the reaction cell together with argon (Ar) to accelerate the water-splitting reaction.[246] In these experiments, the evolution of H_2 and O_2 increased continuously over time. The volume ratio of the evolved gas was $H_2 : O_2 = 2 : 1$. These results indicated that the water-splitting photocatalysis proceeded ideally under the conditions of this gas flow.

Fig. 18 shows the rate of gas evolution over $Au_n/BaLa_4Ti_4O_{15}$ ($n = 10, 15, 18, 25,$ and 39; 0.1 wt% Au) and $Au_{NP}/BaLa_4Ti_4O_{15}$
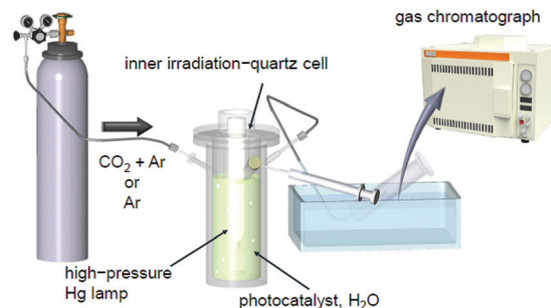

Fig. 17 Schematic of the system used to estimate the photocatalytic activity in our study.[225,232] Reproduced with permission from ref. 247. Copyright 2018 American Chemical Society.

(Au_{NP} = Au NPs) on which 8–22 nm of Au_{NP} was loaded by photodeposition. As shown in Fig. 18, the amount of gas increased continuously with a decreasing number of constituent atoms.[232] This finding indicates that $Au_n/BaLa_4Ti_4O_{15}$ loaded with smaller sized Au_n NCs has higher photocatalytic activity for $Au_n/BaLa_4Ti_4O_{15}$ with the same amount (wt%) of Au. Because the increase in activity with a decreasing number of constituent atoms is very gradual, the change in activity between them is interpreted to be mainly caused by the change in the ratio of surface Au atoms, $i.e.$, the change in the number of Au atoms that can react with protons (H^+).

On the other hand, the difference in photocatalytic activity between $Au_n/BaLa_4Ti_4O_{15}$ and $Au_{NP}/BaLa_4Ti_4O_{15}$ cannot be explained by the difference in the number of surface atoms alone. Various analyses have shown that the activity per surface Au atom was reduced by 75–85% in $Au_{10}/BaLa_4Ti_4O_{15}$ compared with in $Au_{NP}/BaLa_4Ti_4O_{15}$.[232] This finding suggests that the increase in activity by the ultra-miniaturization of the Au cocatalyst (Au NPs → Au_n NCs) (Fig. 18) is mainly caused by the increase in the number of surface Au atoms, which exceeds the decrease in activity per Au atom.

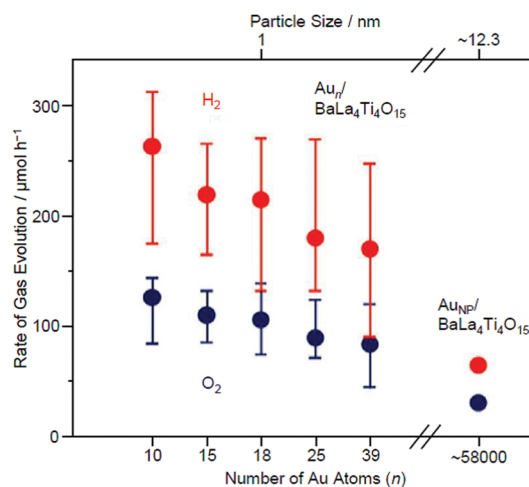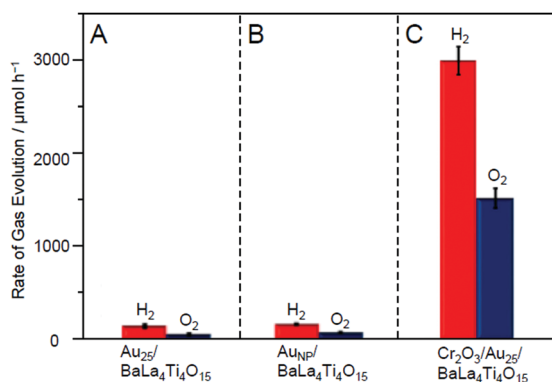**Fig. 18** Effect of the NC size on the water-splitting activity studied using $Au_n/BaLa_4Ti_4O_{15}$ (n = 10, 15, 18, 25, and 39) and $Au_{NP}/BaLa_4Ti_4O_{15}$ (0.1 wt% Au). The average values obtained from four measurements are plotted herein. Reproduced with permission from ref. 232. Copyright 2015 American Chemical Society.
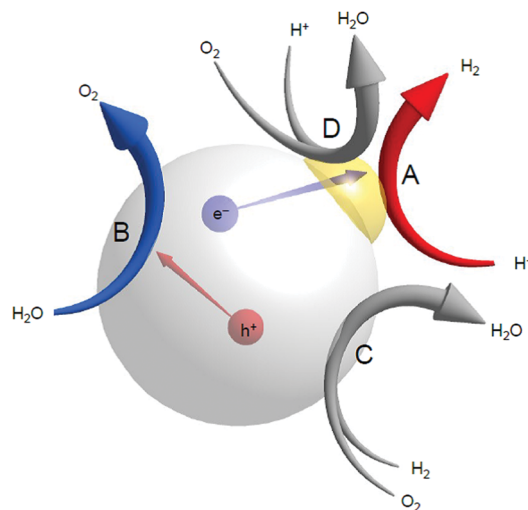
Without flowing CO_2. Although the CO_2 flow in the above-mentioned experiments is an effective means to achieve high activity, the photocatalysts are expected to be dispersed over a large area of water and irradiated with sunlight in practical applications.[38] Therefore, we conducted the same measurements under Ar flow conditions (Fig. 17).[247] The results revealed that the presence of CO_2 affects not only the water-splitting activity but also its dependence on the size of the Au cocatalyst.

Fig. 19A and B show the rate of gas evolution for $Au_{25}/BaLa_4Ti_4O_{15}$ and $Au_{NP}/BaLa_4Ti_4O_{15}$ under an Ar flow (without CO_2). The ratio of H_2 to O_2 evolution was close to 2:1 regardless of the type of photocatalyst ($Au_{25}/BaLa_4Ti_4O_{15}$ or $Au_{NP}/BaLa_4Ti_4O_{15}$), confirming that the water-splitting reaction proceeded ideally. However, under this flow condition, there was no significant difference in the water-splitting activity between $Au_{25}/BaLa_4Ti_4O_{15}$ and $Au_{NP}/BaLa_4Ti_4O_{15}$. This finding indicates that the size effect of the cocatalyst varies depending on the type of flowing gas and that the water-splitting activity cannot be improved by mere miniaturization of the Au cocatalyst in the absence of a CO_2 flow.

The water-splitting reaction consists of multiple reactions (Fig. 20). Therefore, we investigated how the miniaturization of the Au cocatalyst affects each reaction. First, we examined the HER (Fig. 20A). The results revealed that the miniaturization of Au cocatalysts accelerate the HER. However, as mentioned above, the water-splitting activity was not improved by miniaturization of the Au cocatalyst. Thus, we next investigated the effect of the miniaturization of Au cocatalysts on the reverse reaction. The results indicated that the miniaturization of the Au cocatalyst also accelerates one of the reverse reactions, the O_2-photoreduction reaction (Fig. 20D). It was thus interpreted that under an Ar flow, the water-splitting activity cannot be enhanced by mere miniaturization of the Au cocatalyst as it causes the acceleration of both reactions, thereby cancelling the acceleration effect.[247]
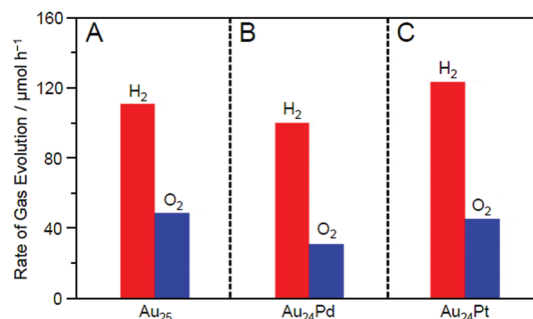

Fig. 20 Possible reactions that occur over a water-splitting photocatalyst during the photocatalytic reaction: (A) the HER, (B) the OER, (C) the reverse reaction, and (D) O_2 photoreduction.

3.3.2. Effect of heteroatom substitution. We also studied the effect of heteroatom substitutions on the water-splitting activity using $Au_{25}/BaLa_4Ti_4O_{15}$, $Au_{24}Pd/BaLa_4Ti_4O_{15}$, and $Au_{24}Pt/BaLa_4Ti_4O_{15}$.[233] In this experiment, the measurements were also performed under the condition that only Ar was flowed.

Fig. 21 shows the amounts of H_2 and O_2 evolved over $Au_{25}/BaLa_4Ti_4O_{15}$, $Au_{24}Pd/BaLa_4Ti_4O_{15}$, and $Au_{24}Pt/BaLa_4Ti_4O_{15}$. The amount of evolved gas was higher in the order of $Au_{24}Pd/BaLa_4Ti_4O_{15} < Au_{25}/BaLa_4Ti_4O_{15} < Au_{24}Pt/BaLa_4Ti_4O_{15}$. This result demonstrates that the substitution of one Au atom of $Au_{25}/BaLa_4Ti_4O_{15}$ with Pd causes a decrease in the water-splitting activity, whereas the substitution of one Au atom of $Au_{25}/BaLa_4Ti_4O_{15}$ with Pt induces an increase in the water-splitting activity. Such an enhancement of the water-splitting activity by Pt substitution has also been observed in the work of another group,[248–250] where larger Au–Pt alloy NPs were used as cocatalysts. Fig. 21 demonstrates that such an effect occurs

Fig. 19 Comparison of the rates of H_2 and O_2 evolution by photocatalytic water-splitting over (A) $Au_{25}/BaLa_4Ti_4O_{15}$, (B) $Au_{NP}/BaLa_4Ti_4O_{15}$, and (C) $Cr_2O_3/Au_{25}/BaLa_4Ti_4O_{15}$ (0.1 wt% Au; 0.5 wt% Cr). Averages of values obtained from several experiments are shown. Reproduced with permission from ref. 247. Copyright 2018 American Chemical Society.

Fig. 21 Rates of H_2 and O_2 evolution by photocatalytic water-splitting with $Au_{24}M/BaLa_4Ti_4O_{15}$ for M = (A) Au, (B) Pd, and (C) Pt (~0.1 wt% M; all the samples include the same number of metal atoms in the cocatalysts). The averages of the values obtained from three experiments are used in the figures. Reproduced with permission from ref. 233. Copyright 2019 American Chemical Society.

with only single atom substitution of the cocatalyst for Au_{25}/$BaLa_4Ti_4O_{15}$.

To elucidate the reason for this change in the water-splitting activity, we investigated the effect of heteroatom substitutions on each reaction over the photocatalyst (Fig. 20).[233] The results indicated that both heteroatom substitutions accelerated the H_2 evolution (Fig. 22). These substitutions were also observed to accelerate the O_2 photoreduction, especially for the Pd substitution. From these results, it can be interpreted that the water-splitting activity was reduced by Pd substitution because its effect on the acceleration of O_2 photoreduction exceeded its effect on the enhancement of H_2 evolution, whereas the water-splitting activity was increased by Pt substitution because the effect of improving H_2 evolution exceeded the effect of promoting O_2 photoreduction (Fig. 22).

Thus, the Pd and Pt substitutions induce different effects on the reactions that occur on the photocatalyst, respectively. This appears to be largely related to the different substitution positions of both elements. As mentioned above, both Pd and Pt substitutions increase the electron density of Au (Fig. 15). Because both H_2 production and O_2 photoreduction require electrons (Fig. 20), this increase in the electron density of Au appears to cause an increase in the reaction rates of both reactions (Fig. 22B and C).

However, in $Au_{24}Pd$/$BaLa_4Ti_4O_{15}$, Pd, which more easily reduces O_2 than Au, is located on the surface of the alloy NCs (Fig. 22B). Pd was bound to S immediately after the photocatalyst preparation (Fig. 16B). However, after light irradiation, S appears to be reduced to H_2S and then desorbed from the surface of the metal NCs. Thus, Pd is presumed to be exposed during the water-splitting reaction (Fig. 22B). The presence of such bare Pd is expected to greatly accelerate the O_2 photoreduction over $Au_{24}Pd$/$BaLa_4Ti_4O_{15}$. This appears to be the reason why the effect of Pd substitution on the acceleration of O_2 photoreduction exceeded the effect on the enhancement of H_2 evolution.

For $Au_{24}Pt$/$BaLa_4Ti_4O_{15}$, the Pt is located at the interface between the alloy NCs and $BaLa_4Ti_4O_{15}$ (Fig. 16C); thus, Pt is not exposed during the water-splitting reaction. In addition, because electron transfer occurs more easily via Pt atoms than via Au atoms at the interface, it is expected that photoexcited electrons are more efficiently transferred from $BaLa_4Ti_4O_{15}$ to metal NCs in $Au_{24}Pt$/$BaLa_4Ti_4O_{15}$ than in $Au_{24}Pd$/$BaLa_4Ti_4O_{15}$ (and Au_{25}/$BaLa_4Ti_4O_{15}$) (Fig. 22C). These facts appear to be

largely related to the difference in the heteroatom substitution effect between Pd and Pt substitutions.

3.4. Creation of highly active water-splitting photocatalysts

In this way, the establishment of the atomically precise control technique of cocatalysts provided a deeper understanding of (i) the electronic/geometric structure of cocatalysts, (ii) the binding mode at the interface between the cocatalysts and photocatalysts, and (iii) the effect of the number of constituent atoms of the cocatalysts and the alloying on the catalytic activities. We have also attempted to create highly active water-splitting photocatalysts based on this knowledge.

3.4.1. Formation of a chromium oxide shell on cocatalysts for suppressing the reverse reaction. As described in Section 3.3.1, decreasing the particle size of Au cocatalysts accelerates the HER. Substituting one Au atom of the Au cocatalysts with Pd or Pt further accelerates the HER. However, these modifications also accelerate the O_2-photoreduction reaction. Based on this knowledge, it can be expected that if we could suppress the reverse reaction, a highly active water-splitting photocatalyst could be created based on the characteristic of fine Au_n NC and heteroatom-doped Au_n NC cocatalysts, namely, high H_2-evolution activity.

One effective means to suppress the reverse reaction of water splitting is to form a chromium oxide (Cr_2O_3) shell on the surface of the loaded cocatalyst. The Cr_2O_3 shell is permeable to H^+ but not to O_2 approaching from the outside. Domen et al. reported that when the cocatalyst surface is covered by a Cr_2O_3 shell with such characteristics, it is possible to suppress only the progress of the reverse reaction while maintaining the H_2-evolution activity. Thus, this approach is effective for improving the water-splitting activity.[38,146,219–221,251–256] In their research, they used the photodeposition method to form the Cr_2O_3 shell (Fig. 23A). However, when Au_{25}/$BaLa_4Ti_4O_{15}$, $Au_{24}Pd$/$BaLa_4Ti_4O_{15}$, and $Au_{24}Pt$/$BaLa_4Ti_4O_{15}$ were irradiated with UV light, the loaded metal NCs aggregated.[233] Thus, when the method reported by Domen et al. is used as is, it is difficult to form the Cr_2O_3 shell on the surface of the loaded metal NCs while maintaining the number of atoms of the metal NCs. However, research in the field of surface science has revealed that when a metal oxide loaded with metal NPs is heated under an H_2 or O_2 atmosphere, a strong metal–support interaction (SMSI) is induced, thereby leading to the formation of an oxide film on the metal NPs.[257–264] Therefore, we attempted to form a Cr_2O_3 shell on the surface of the metal NC cocatalyst using such a SMSI effect (Fig. 23B).[247]

Au_{25}/$BaLa_4Ti_4O_{15}$. In our Cr_2O_3 shell formation process, the Cr_2O_3 layer was first formed on $BaLa_4Ti_4O_{15}$ using the photodeposition method before loading Au_{25}. Fig. 24A and B present TEM and HR-TEM images of the photocatalysts on which the Cr_2O_3 (0.5 wt% Cr) layer was formed. These images confirm that Cr_2O_3 layers with thicknesses of approximately 0.7–1.3 nm were formed on $BaLa_4Ti_4O_{15}$. Then, $Au_{25}(SG)_{18}$ was adsorbed onto the obtained Cr_2O_3/$BaLa_4Ti_4O_{15}$ (0.1 wt% Au; Fig. 24C and D). The photocatalyst after the adsorption of $Au_{25}(SG)_{18}$

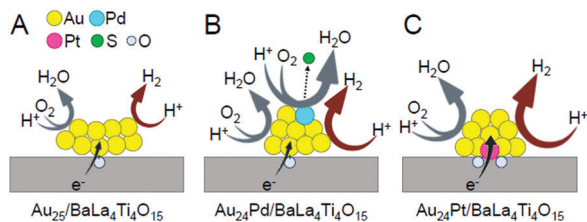**Fig. 22** Proposed structures of $Au_{24}M$/$BaLa_4Ti_4O_{15}$ for M = (A) Au, (B) Pd, and (C) Pt during the water-splitting reaction. Reproduced with permission from ref. 233. Copyright 2019 American Chemical Society.
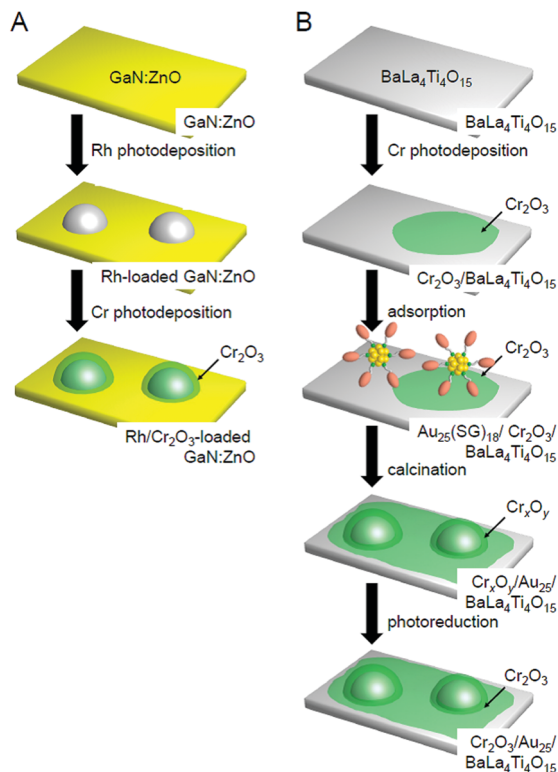
Fig. 23 Comparison of the procedures of Cr_2O_3 shell formation in (A) the literature[254] and (B) our work.[247] Reproduced with permission from ref. 247 and 254. Copyright 2018 American Chemical Society and Copyright 2006 Wiley-VCH.

Fig. 24 TEM images (A, C and E) and HR-TEM images (B, D and F) of (A and B) $Cr_2O_3/BaLa_4Ti_4O_{15}$ (0.5 wt% Cr), (C and D) $Au_{25}(SG)_{18}/Cr_2O_3/BaLa_4Ti_4O_{15}$ (0.1 wt% Au; 0.5 wt% Cr), and (E and F) $Cr_2O_y/Au_{25}/BaLa_4Ti_4O_{15}$ (0.1 wt% Au; 0.5 wt% Cr). Cr_2O_y indicates the chromium oxide in which part of the chromium was oxidized to a highly oxidized state ($>3+$). In (C and E), the insets show the core-size distributions of the particles. In (B and F), the thicknesses of the Cr_2O_3 or Cr_2O_y shells are indicated by yellow double-pointed arrows. In part (F), the particle size is also indicated by a white double-pointed arrow. Reproduced with permission from ref. 247. Copyright 2018 American Chemical Society.

($Au_{25}(SG)_{18}/Cr_2O_3/BaLa_4Ti_4O_{15}$) was calcined at 300 °C for 2 h under a reduced pressure. In the TEM image of the photocatalyst after calcination (Fig. 24E), particles with an average size of 1.1 ± 0.3 nm were observed. In the HR-TEM image of the photocatalyst after calcination (Fig. 24F), a thin layer with a thickness of approximately 0.7–0.9 nm was observed around particles with high electron density. This indicates that the Au_{25} was covered with a Cr_2O_3 layer during calcination (Fig. 23B). Part of the chromium was oxidized to a highly oxidized state ($>3+$) during calcination. Accordingly, we irradiated the photocatalyst with UV light to reduce the highly oxidized chromium oxide to Cr_2O_3 and thereby obtain the desired $Cr_2O_3/Au_{25}/BaLa_4Ti_4O_{15}$.[247]

The resulting $Cr_2O_3/Au_{25}/BaLa_4Ti_4O_{15}$ exhibited higher water-splitting activity than $Au_{25}/BaLa_4Ti_4O_{15}$. Fig. 19A and C show the water-splitting activity of $Au_{25}/BaLa_4Ti_4O_{15}$ and $Cr_2O_3/Au_{25}/BaLa_4Ti_4O_{15}$. $Au_{25}/BaLa_4Ti_4O_{15}$, without a Cr_2O_3 shell, evolved H_2 at 160.5 μmol h^{-1} (Fig. 19A). On the other hand, $Cr_2O_3/Au_{25}/BaLa_4Ti_4O_{15}$, which had a Cr_2O_3 shell, evolved H_2 at 3032 μmol h^{-1} (Fig. 19C). These results demonstrate that forming the Cr_2O_3 shell enhanced the water-splitting activity of the photocatalyst by approximately 19 times. Cr_2O_3 itself hardly improved the water-splitting activity.[247] In addition, forming the Cr_2O_3 shell had little effect on the electronic state of Au_{25}.[247] Therefore, it can be considered that the improvement in the water-splitting activity was mainly caused by the suppression of the O_2-photoreduction reaction due to the Cr_2O_3 shell formation. Indeed, it was experimentally confirmed that
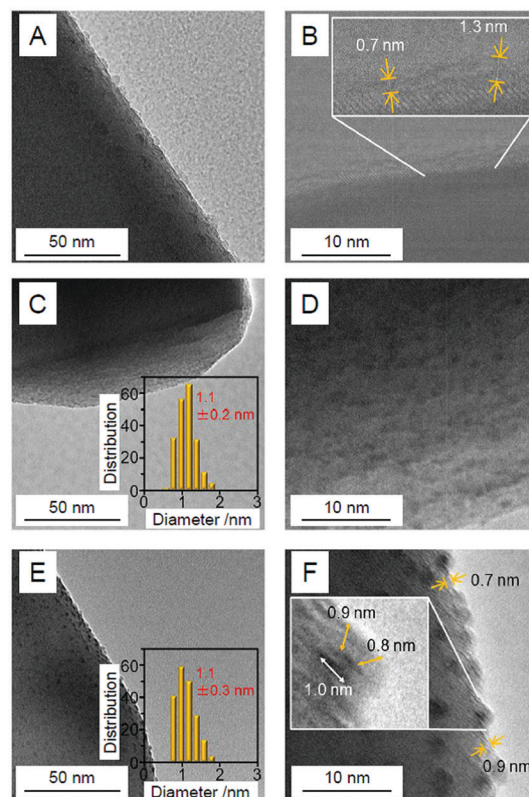
the O_2-photoreduction reaction was greatly suppressed over $Cr_2O_3/Au_{25}/BaLa_4Ti_4O_{15}$.[247] In this way, we succeeded in creating a highly active water-splitting photocatalyst that takes advantage of Au_{25} cocatalysts by forming a Cr_2O_3 shell on the surface of the Au_{25} cocatalysts.

This study also revealed that the aggregation of cocatalysts during light irradiation can be suppressed by forming the Cr_2O_3 shell.[247] When using our Cr_2O_3-shell formation method, Au_{25} was covered with a Cr_2O_3 layer on $BaLa_4Ti_4O_{15}$ (Fig. 23B). In this case, Au_{25} should not easily move around on the surface of the photocatalysts. Indeed, $Cr_2O_3/Au_{25}/BaLa_4Ti_4O_{15}$ maintained high water-splitting activity for a long time (Fig. 25A). Unlike for $Au_{25}/BaLa_4Ti_4O_{15}$ (Fig. 25B(a)), the particle size of the Au cocatalyst hardly changed even after 10 h light-irradiation for $Cr_2O_3/Au_{25}/BaLa_4Ti_4O_{15}$ (Fig. 25B(b)). These results indicate that the Cr_2O_3 shell formed using our method improves not only the water-splitting activity but also the stability of the cocatalyst on the photocatalyst surface.

$Au_{24}Pt/BaLa_4Ti_4O_{15}$. We also attempted to form the Cr_2O_3 shell on $Au_{24}Pt/BaLa_4Ti_4O_{15}$ using a similar method to that
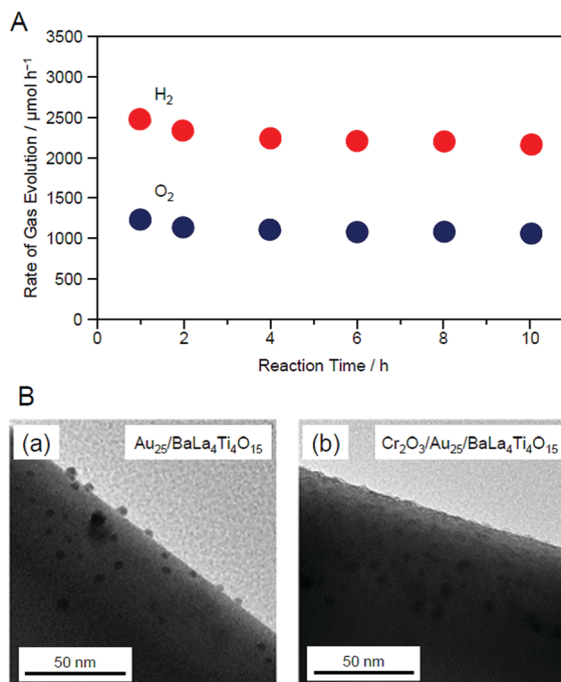
Fig. 25 (A) Time dependence of the evolution of H_2 and O_2 over Cr_2O_3/Au_{25}/$BaLa_4Ti_4O_{15}$ with 0.1 wt% Au and 0.5 wt% Cr. (B) TEM images of (a) Au_{25}/$BaLa_4Ti_4O_{15}$ and (b) Cr_2O_3/Au_{25}/$BaLa_4Ti_4O_{15}$ after UV irradiation for 10 h. Reproduced with permission from ref. 247. Copyright 2018 American Chemical Society.

Fig. 26 (A and B) (a) TEM images and particle-size distributions and (b) HR-TEM images of Cr_2O_3/$(Au_{24}Pt)_{1-3}$/$BaLa_4Ti_4O_{15}$ ($\sim$0.1 wt% M (M = Au or Pt); 0.3 wt% Cr) before (A) and after (B) UV light irradiation for 10 h. The thicknesses of the Cr_2O_3 shells and the particle sizes are indicated by black and yellow double-ended arrows, respectively. Reproduced with permission from ref. 233. Copyright 2019 American Chemical Society.

shown in Fig. 23B.[233] Fig. 26A presents TEM and HR-TEM images of the obtained photocatalyst, respectively. In the TEM image, particles of 1.3 ± 0.3 nm in size were observed. This particle size was slightly larger than that of $Au_{24}Pt$-$(PET)_{18-y}$(p-MBA)$_y$/Cr_2O_3/$BaLa_4Ti_4O_{15}$ (1.0 ± 0.2 nm). This indicates that for $Au_{24}Pt$/$BaLa_4Ti_4O_{15}$, slight aggregation of the cocatalysts occurred during Cr_2O_3 shell formation. Based on the particle-size distribution (Fig. 26A(a)), the main product was estimated to be $(Au_{24}Pt)_{1-3}$ composed of 1–3 $Au_{24}Pt$ units, meaning that $\sim$77% of the $Au_{24}Pt$ was aggregated to form $(Au_{24}Pt)_{2,3}$.[233] p-MBA has a smaller number of hydrophilic functional groups than SG. Furthermore, in Au_{24}-$Pt(PET)_{18-y}$(p-MBA)$_y$(y = 3–10), not all the ligands have hydrophilic functional groups. Therefore, $Au_{24}Pt(PET)_{18-y}$(p-MBA)$_y$ (y = 3–10) should more weakly adsorb to the Cr_2O_3 surface than $Au_{25}(SG)_{18}$. It can be considered that slight aggregation of $Au_{24}Pt$ occurred during calcination, most likely due to this weaker adsorption. The HR-TEM images confirmed that the Cr_2O_3 layer was also formed around $(Au_{24}Pt)_{1-3}$ (Fig. 26A(b)).

Fig. 27 shows the amount of gas evolved over Cr_2O_3/$(Au_{24}Pt)_{1-3}$/$BaLa_4Ti_4O_{15}$. This photocatalyst evolved approximately 20 times more gas than $Au_{24}Pt$/$BaLa_4Ti_4O_{15}$ (Fig. 27),[233] indicating that Cr_2O_3/$(Au_{24}Pt)_{1-3}$/$BaLa_4Ti_4O_{15}$ was even more active than $Au_{24}Pt$/$BaLa_4Ti_4O_{15}$. In addition, the total amount of gas increased proportionally with time. After light irradiation, the average particle size slightly increased compared with that of Cr_2O_3/$(Au_{24}Pt)_{1-3}$/$BaLa_4Ti_4O_{15}$ before light irradiation (Fig. 26B(a)). However, the increase in particle size

Fig. 27 Time course of water splitting over Cr_2O_3/$(Au_{24}Pt)_{1-3}$/$BaLa_4Ti_4O_{15}$ together with that over $Au_{24}Pt$/$BaLa_4Ti_4O_{15}$. Reproduced with permission from ref. 233. Copyright 2019 American Chemical Society.

(1.3 ± 0.3 nm → 1.6 ± 0.6 nm) was far more suppressed than for $Au_{24}Pt$/$BaLa_4Ti_4O_{15}$ without the Cr_2O_3 layer (1.1 ± 0.2 nm → 2.8 ± 0.9 nm). These results suggest that the combination of Pt substitution and Cr_2O_3 layer formation makes it possible to create highly active and stable photocatalysts.

In this way, we have succeeded in forming a Cr_2O_3 layer on $(Au_{24}Pt)_{1-3}$ and thereby creating a photocatalyst with high activity and stability. Unfortunately, for $Au_{24}Pt$, $\sim$77% of the $Au_{24}Pt$ aggregated during formation of the Cr_2O_3 layer. Furthermore, there was a slight increase in the particle size after 10 h of the water-splitting reaction, even for the photocatalyst with a Cr_2O_3 layer. This increase is most likely because all of the alloy clusters were not necessarily covered with a Cr_2O_3 layer.

However, if these problems could be addressed, more functional photocatalysts will be successfully created through a combination of decreasing the particle size, alloying, and suppressing the reverse reaction by Cr_2O_3-layer formation.

3.4.2. Use of rhodium. In the above series of studies, Au was used as the base element of the cocatalyst NCs. However, a volcano plot of H^+ adsorption/H_2 desorption[265] predicts that Rh should exhibit higher activity than Au as a cocatalyst for the HER. Therefore, loading an ultrafine cocatalyst composed of Rh and Cr oxides onto a photocatalyst surface is expected to induce higher water-splitting activity. Indeed, Domen *et al.* reported that photocatalysts loaded with Rh^{III}–Cr^{III} mixed-oxide NPs ($Rh_{2-x}Cr_xO_3$, 10–30 nm) exhibited higher water-splitting activity than those loaded with metal NPs composed of other metal elements.[266–269] The activity of the photocatalysts is expected to increase with the use of finer $Rh_{2-x}Cr_xO_3$ NPs. However, it is difficult to load ultrafine $Rh_{2-x}Cr_xO_3$ particles onto photocatalysts using conventional methods (Fig. 3A and B). Accordingly, we attempted to load fine $Rh_{2-x}Cr_xO_3$ NCs on $BaLa_4Ti_4O_{15}$ using our method (Fig. 28).[270]

Unfortunately, there have been no reports on the precise synthesis of $Rh_{2-x}Cr_xO_3$ NCs. Therefore, in this experiment, Rh–SG complexes, containing $Rh_2(SG)_2$ as a main component, were used as a precursor. First, the Cr_2O_3 layer was formed on $BaLa_4Ti_4O_{15}$ by photodeposition to prepare $Cr_2O_3/BaLa_4Ti_4O_{15}$ (Fig. 29A). Then, the Rh–SG complexes were adsorbed on the surface of $Cr_2O_3/BaLa_4Ti_4O_{15}$ (Fig. 29B(a)). Various structural analyses revealed that approximately 6 $Rh_2(SG)_2$ complexes aggregated during adsorption.[270] Then, Rh–SG/$Cr_2O_3/BaLa_4Ti_4O_{15}$ was calcined at 300 °C under reduced pressure to remove the ligands from the Rh–SG complexes and form a solid solution of Rh and Cr oxides (Fig. 29B and C). Finally, a small amount of Cr with a slightly higher oxidation state was reduced to Cr^{III} by UV light irradiation (Fig. 28E). This series of procedures enabled us to load $Rh_{2-x}Cr_xO_3$ NCs with sizes of approximately 1.3 ± 0.3 nm and a narrow size distribution on $BaLa_4Ti_4O_{15}$ ($Rh_{2-x}Cr_xO_3/BaLa_4Ti_4O_{15}$; Fig. 29D(a)).
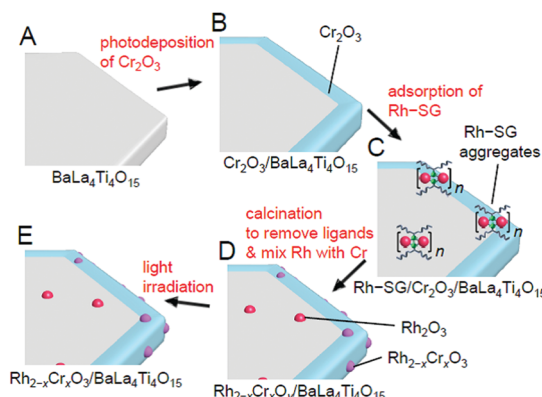
Fig. 28 Schematic of the experimental procedure for the formation of $Rh_{2-x}Cr_xO_3/BaLa_4Ti_4O_{15}$. (A) $BaLa_4Ti_4O_{15}$, (B) $Cr_2O_3/BaLa_4Ti_4O_{15}$, (C) Rh–SG/$Cr_2O_3/BaLa_4Ti_4O_{15}$, (D) $Rh_{2-x}Cr_xO_y/BaLa_4Ti_4O_{15}$, and (E) $Rh_{2-x}Cr_xO_3/BaLa_4Ti_4O_{15}$. $Rh_{2-x}Cr_xO_y$ indicates $Rh_{2-x}Cr_xO_3$ including highly oxidized Cr (>3+). Reproduced with permission from ref. 270. Copyright 2020 Wiley-VCH.
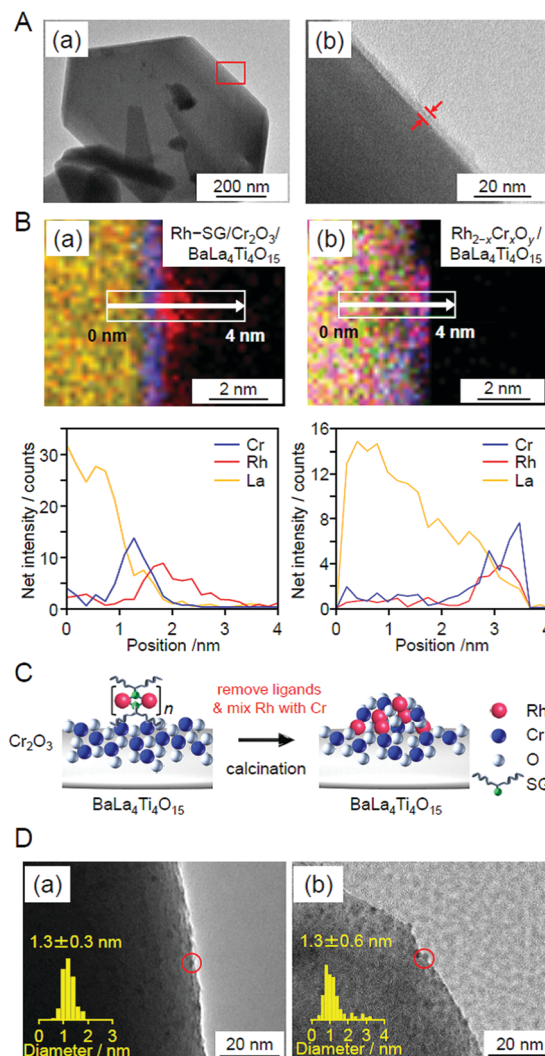
Fig. 29 (A) HR-TEM images of $Cr_2O_3/BaLa_4Ti_4O_{15}$ observed at (a) low magnification and (b) high magnification for the edge of $BaLa_4Ti_4O_{15}$. The image in (b) is an expansion of the red square in the image in (a). In this experiment, Cr was loaded at 1 wt% to easily monitor the position of the Cr_2O_3 layers. (B) Line analysis of elemental mapping for (a) Rh–SG/$Cr_2O_3/BaLa_4Ti_4O_{15}$ and (b) $Rh_{2-x}Cr_xO_y/BaLa_4Ti_4O_{15}$. (C) Schematic of the phenomenon that occurred during the calcination process. (D) TEM images of $Rh_{2-x}Cr_xO_3/BaLa_4Ti_4O_{15}$ (a) before and (b) after UV irradiation for 10 h. The red circles indicate the $Rh_{2-x}Cr_xO_3$ particles. Reproduced with permission from ref. 270. Copyright 2020 Wiley-VCH.

The obtained photocatalyst exhibited an apparent quantum yield of 16% (excitation wavelength = 270 nm; Fig. 30), which is the highest achieved for $BaLa_4Ti_4O_{15}$ to date.[270] For this photocatalyst, almost no decrease in activity and no increase in particle size were observed even after 10 h of the water-splitting reaction (Fig. 29D(b)). Moreover, it was confirmed that both the reverse reaction (Fig. 20C) and O_2-photoreduction reaction (Fig. 20D) were well suppressed over this sample, as expected.[270] These results indicate that loading $Rh_{2-x}Cr_xO_3$ NCs using our method is very effective for creating highly functional water-splitting photocatalysts.

The method of loading $Rh_{2-x}Cr_xO_3$ NCs established in this study can be applied to other photocatalysts in principle.
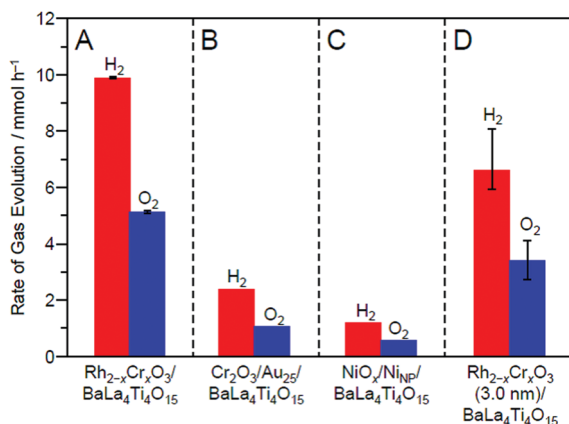
Fig. 30 Comparison of the rates of H_2 and O_2 evolution by photocatalytic water-splitting over different photocatalysts: (A) $Rh_{2-x}Cr_xO_3$/$BaLa_4Ti_4O_{15}$ (0.09 wt% Rh and 0.10 wt% Cr), (B) Cr_2O_3/Au_{25}/$BaLa_4Ti_4O_{15}$ (0.10 wt% Au and 0.50 wt% Cr), (C) NiO_x/Ni_{NP}/$BaLa_4Ti_4O_{15}$ (0.50 wt% Ni), and (D) $Rh_{2-x}Cr_xO_3$ (3.0 nm)/$BaLa_4Ti_4O_{15}$ (0.10 wt% Rh and 0.15 wt% Cr). In this study, NiO_x/Ni_{NP}/$BaLa_4Ti_4O_{15}$ and $Rh_{2-x}Cr_xO_3$ (3.0 nm)/$BaLa_4Ti_4O_{15}$ loaded with $Rh_{2-x}Cr_xO_3$ NPs of ∼3.0 nm were prepared by the impregnation method. Reproduced with permission from ref. 270. Copyright 2020 Wiley-VCH.

In addition, $Rh_{2-x}Cr_xO_3$ is an effective cocatalyst for various water-splitting photocatalysts.[266–269,271,272] In the future, it is expected that high quantum yields can be achieved for many water-splitting photocatalysts using this loading method.

4. Conclusions

We have attempted to create practical water-splitting photocatalysts by combining the most advanced techniques of both metal NCs and water-splitting photocatalysts (Fig. 4). The following findings were obtained regarding the loading of an atomically precise cocatalyst, the electronic/geometric structure of a cocatalyst, the correlation between the types of loaded metal NCs and the water-splitting activity, and the functionalization of a water-splitting photocatalyst.

Loading of atomically precise metal NCs

(i) When $Au_n(SG)_m$ NCs are used as precursors, it is possible to load Au_n NCs with a controlled number of constituent atoms on $BaLa_4Ti_4O_{15}$ and $SrTiO_3$.

(ii) To load Au_n NCs while maintaining the number of constituent atoms of the precursor NCs, it is indispensable to use $Au_n(SG)_m$ NCs with high stability in solution as the precursor.

(iii) If hydrophobic metal NCs are used as precursors, replacing some of the ligands of the NCs with hydrophilic ligands via ligand exchange is an effective means of loading atomically precise metal NCs on the photocatalyst.

(iv) An increase in the amount of loaded NCs induces an increase in the particle size of the loaded NCs. In the loading of Au_n (n = 10, 15, 18, 25, or 39), $Au_{24}Pd$, and $Au_{24}Pt$ on $BaLa_4Ti_4O_{15}$, when metal NCs are loaded with < 0.2 wt% metal, it is possible to suppress the aggregation of NCs on the photocatalysts.

Electronic structures

(i) The loaded metal NCs have electronic structures different from those of the precursor metal NCs.

(ii) In Au_{25}/$BaLa_4Ti_4O_{15}$, partial charge transfer occurs from $BaLa_4Ti_4O_{15}$ to Au_{25}.

(iii) Substitution of Au in Au_{25}/$BaLa_4Ti_4O_{15}$ with Pd or Pt increases the electron density of Au in the loaded NCs.

Geometric structures

(i) On $BaLa_4Ti_4O_{15}$, Au_{25} NCs have a relatively planar geometric structure, and $Au_{24}Pd$ and $Au_{24}Pt$ NCs have more three-dimensional structures.

(ii) In $Au_{24}Pd$/$BaLa_4Ti_4O_{15}$, Pd is located on the surface of the loaded metal NCs and bound to S. On the other hand, in $Au_{24}Pt$/$BaLa_4Ti_4O_{15}$, Pt is located at the interface between $Au_{24}Pt$ NCs and $BaLa_4Ti_4O_{15}$.

(iii) In Au_{25}/$BaLa_4Ti_4O_{15}$ and $Au_{24}Pd$/$BaLa_4Ti_4O_{15}$, there are only a few Au–O bonds at the interface between the metal NCs and the photocatalyst, leading to the weak immobilization of the loaded metal NCs on the photocatalyst. On the other hand, in $Au_{24}Pt$/$BaLa_4Ti_4O_{15}$, several Pt–O bonds are formed at the interface of the metal NC/photocatalyst, leading to stronger immobilization of the loaded metal NCs on the photocatalyst.

Catalytic activity

(i) With the same Au loading amount, Au_n/$BaLa_4Ti_4O_{15}$ with a smaller number of constituent atoms exhibits higher photocatalytic activity.

(ii) The difference in activity among Au_n/$BaLa_4Ti_4O_{15}$ (n = 10, 15, 18, 25, and 39; 0.1 wt% Au) is mainly due to the change in the proportion of surface Au atoms.

(iii) The higher activity of Au_n/$BaLa_4Ti_4O_{15}$ compared with Au_{NP}/$BaLa_4Ti_4O_{15}$ is caused by the increase in the number of surface Au atoms that exceeds the decrease in activity per Au atom.

(iv) The size effect of the cocatalyst changes depending on the type of flowing gas. When using flowing gas not containing CO_2, the water-splitting activity is not changed by mere miniaturization of the Au cocatalyst. This phenomenon is explained by the acceleration of both the HER and O_2-reduction reaction due to miniaturization of the Au cocatalyst.

(v) The substitution of one Au of Au_{25}/$BaLa_4Ti_4O_{15}$ with Pd induces a decrease in the water-splitting activity. On the other hand, the substitution of one Au of Au_{25}/$BaLa_4Ti_4O_{15}$ with Pt induces an increase in the water-splitting activity. These opposite trends are caused by the difference in the substitution positions of Pd and Pt.

Functionalization

(i) A highly active water-splitting photocatalyst that takes advantage of the high H_2-production ability of ultrafine Au_n NCs can be created by forming a Cr_2O_3 shell on the surface of Au_n NCs. When applying Pt substitution to such cocatalysts, further high water-splitting activity can be obtained.

(ii) When using fine $Rh_{2-x}Cr_xO_3$ NCs as a cocatalyst, further enhancement of the activity can be achieved for $BaLa_4Ti_4O_{15}$ photocatalysts.

It is expected that these findings will lead to clear design guidelines for the creation of practical water-splitting photocatalysts.

5. Outlook

The following efforts are considered necessary to obtain a deeper knowledge of water-splitting photocatalysts and thereby create practical photocatalysts.

Establishment of a synthesis method of atomically precise Rh_n NCs

The study on $Au_n/BaLa_4Ti_4O_{15}$, where the number of constituent atoms of the cocatalyst was controlled with atomic precision, revealed the details of the effect of miniaturization of the Au cocatalyst on each reaction. However, although the number of constituent atoms of the cocatalyst was not controlled with atomic precision, even higher water-splitting activity was achieved for $Rh_{2-x}Cr_xO_3$ NC/$BaLa_4Ti_4O_{15}$. Therefore, precise synthesis methods are expected to be established for Rh_n NCs in the future. If the obtained precise Rh_n NCs would be used as precursors of cocatalysts, we could obtain deeper understanding of the functionalization of $Rh_{2-x}Cr_xO_3$ NC/$BaLa_4Ti_4O_{15}$ and thereby create even more active $Rh_{2-x}Cr_xO_3$ NC/$BaLa_4Ti_4O_{15}$.

Use of non-noble metal cocatalysts

As shown in this feature article, the use of cocatalysts consisting of noble metals, such as Au, Pt, and Rh, is effective for producing high activity. However, these metals are expensive elements. Since previous studies showed that non-noble elements, such as nickel, cobalt, manganese, etc.,[210,222,273] can also be used for the creation of active cocatalysts, research searching for effective non-noble metal cocatalysts is expected to be conducted in future studies. To achieve this, various precise synthesis methods are also expected to be established for non-noble metal NCs.[274]

Selective loading of metal NCs on the optimal crystal plane

In a semiconductor photocatalyst, there are respective crystal planes which electrons and holes generated by photoexcitation can easily reach. If HER and OER cocatalysts could be selectively loaded on such crystal planes, electrons and holes could be efficiently used in the reaction.[37,275] Thus, techniques for selectively loading metal NCs on specific crystal planes are expected to be developed in the future.

Elucidation of the HER and OER activities of existing metal NCs using electrochemical methods

The research field of metal NCs has already realized the precise synthesis of many metal NCs. Among them, there might be metal NCs with electronic structures suitable for HER and OER cocatalysts. Because the HER and OER activity of each metal NC can be estimated by electrochemical measurements,[21] it is expected that electrochemical experiments will be widely conducted for the existing precise metal NCs. These studies could lead to the discovery of novel high-performance cocatalysts.

Elucidation of the geometric structures of loaded metal NCs

To understand the structure–property relationship, it is essential to obtain deeper understanding of the geometrical structure of the loaded metal NCs. Therefore, in the future, it is expected that the geometric structure of the loaded metal NCs will be studied using Cs-corrected TEM[276] and scanning TEM. In addition, operando measurements using X-ray absorption fine structure (XAFS) analysis[277] are also expected to be conducted to obtain a deeper understanding of the geometric structure during the water-splitting reaction.

Structural control of loaded metal NCs

Even if SR-protected metal NCs having no variation in the geometric structure are used as the precursor, there appears to be variation in the geometric structures of the loaded metal NCs. To identify the geometric structures of NCs that create high activity and to selectively load such NCs on the photocatalysts, it is necessary to establish methods to control the geometric structure of the loaded NCs. Previous studies have established various methods to refine the size and structure of SR-protected metal NCs dispersed in solution.[153,158,193,278] In the future, it is expected that methods to refine the size and structure will also be established for the loaded NCs.

Decreasing the size of loaded metal NCs

As shown in Section 3.1.1, decreasing the size of cocatalysts leads to higher activity. Recent studies by another group implied that atomically dispersed metal cocatalysts are also effective for improving water-splitting photocatalysts.[279–281] In the future, it is expected that cocatalysts will be controlled in a smaller size region by using smaller ligand-protected metal clusters[114,282–285] and thereby the effective size of the cocatalysts will be elucidated in more detail.

Elucidation of the charge-transfer rate at the interface between the photocatalysts and cocatalysts

To obtain a highly active water-splitting photocatalyst, it is also important to increase the rate of carrier transfer and the carrier injection efficiency from the photocatalyst to the cocatalyst.[286] However, currently, there is little information on these properties for photocatalysts loaded with fine metal NCs. In the future, it is expected that deeper understanding of the carrier transfer rate and carrier injection efficiency will be obtained through fluorescence lifetime measurements and transient absorption spectroscopy.[66–72] Such information would lead to clearer design guidelines for the creation of high-performance cocatalysts that can effectively transfer excited electrons from photocatalysts to cocatalysts.

Activation of visible-light-responsive photocatalysts

$BaLa_4Ti_4O_{15}$ and $SrTiO_3$ used in our research exhibit high apparent quantum yields and stabilities among ultraviolet light-driven water-splitting photocatalysts (left half part in Fig. 7). However, approximately 40% of solar energy is in the visible-light region. Therefore, effective use of visible light is indispensable for the practical application of water-splitting photocatalysts.[78] Currently, there are only a few semiconductor photocatalysts that can completely split water in one step using visible light, such as GaN:ZnO, g-C_3N_4, *etc.* (right half part in Fig. 7).[78] However, overall water-splitting using visible light can also be achieved by a photocatalytic system that uses a two-step reaction called the Z-scheme, which imitates photosynthesis in plants.[25,26,29,31–34] In the future, it is expected that both of these visible-light-responsive water-splitting photocatalysts will be more activated based on the knowledge obtained in previous studies.

Guidance by DFT calculations

As described above, in recent years, it has become possible to control the chemical composition of cocatalysts with atomic precision. For photocatalysts loaded with such atomically precise cocatalysts, DFT calculations could predict highly functional photocatalytic systems.[287] In the future, it is expected that research aimed at the improvement of the functionality of photocatalysts will shift from trial-and-error experiments to prediction by DFT calculations.

We hope that many water-splitting photocatalysts for practical use will be created by overcoming these issues and that we can welcome a society in which energy and environmental problems have been solved as soon as possible.

Conflicts of interest

There are no conflicts to declare.

Acknowledgements

References

1 R. S. Stein and J. Powers, *The Energy Problem*, World Scientific, Singpore, 2011.
2 Z. W. Seh, J. Kibsgaard, C. F. Dickens, I. Chorkendorff, J. K. Nørskov and T. F. Jaramillo, *Science*, 2017, **355**, eaad4998.
3 A. Fujishima and K. Honda, *Nature*, 1972, **238**, 37–38.
4 K. Kwak, W. Choi, Q. Tang, M. Kim, Y. Lee, D.-e. Jiang and D. Lee, *Nat. Commun.*, 2017, **8**, 14723.
5 S. Zhao, R. Jin, Y. Song, H. Zhang, S. D. House, J. C. Yang and R. Jin, *Small*, 2017, **13**, 1701519.
6 W. Choi, G. Hu, K. Kwak, M. Kim, D.-e. Jiang, J.-P. Choi and D. Lee, *ACS Appl. Mater. Interfaces*, 2018, **10**, 44645–44653.
7 D. Eguchi, M. Sakamoto and T. Teranishi, *Chem. Sci.*, 2018, **9**, 261–265.
8 K. Kwak, W. Choi, Q. Tang, D.-e. Jiang and D. Lee, *J. Mater. Chem. A*, 2018, **6**, 19495–19501.
9 E. J. Popczun, J. R. McKone, C. G. Read, A. J. Biacchi, A. M. Wiltrout, N. S. Lewis and R. E. Schaak, *J. Am. Chem. Soc.*, 2013, **135**, 9267–9270.
10 J. Xie, J. Zhang, S. Li, F. Grote, X. Zhang, H. Zhang, R. Wang, Y. Lei, B. Pan and Y. Xie, *J. Am. Chem. Soc.*, 2013, **135**, 17881–17888.
11 P. Xiao, M. A. Sk, L. Thia, X. Ge, R. J. Lim, J.-Y. Wang, K. H. Lim and X. Wang, *Energy Environ. Sci.*, 2014, **7**, 2624–2629.
12 H. Jin, J. Wang, D. Su, Z. Wei, Z. Pang and Y. Wang, *J. Am. Chem. Soc.*, 2015, **137**, 2688–2694.
13 Y. Du, J. Xiang, K. Ni, Y. Yun, G. Sun, X. Yuan, H. Sheng, Y. Zhu and M. Zhu, *Inorg. Chem. Front.*, 2018, **5**, 2948–2954.
14 C. Jiang, S. J. A. Moniz, A. Wang, T. Zhang and J. Tang, *Chem. Soc. Rev.*, 2017, **46**, 4645–4660.
15 M. G. Walter, E. L. Warren, J. R. McKone, S. W. Boettcher, Q. Mi, E. A. Santori and N. S. Lewis, *Chem. Rev.*, 2010, **110**, 6446–6473.
16 W. Chen and S. Chen, *Angew. Chem., Int. Ed.*, 2009, **48**, 4386–4389.
17 Y. Lu, Y. Jiang, X. Gao and W. Chen, *Chem. Commun.*, 2014, **50**, 8464–8467.
18 L. Wang, Z. Tang, W. Yan, H. Yang, Q. Wang and S. Chen, *ACS Appl. Mater. Interfaces*, 2016, **8**, 20635–20641.
19 L. Sumner, N. A. Sakthivel, H. Schrock, K. Artyushkova, A. Dass and S. Chakraborty, *J. Phys. Chem. C*, 2018, **122**, 24809–24817.
20 T. C. Jones, L. Sumner, G. Ramakrishna, M. b. Hatshan, A. Abuhagr, S. Chakraborty and A. Dass, *J. Phys. Chem. C*, 2018, **122**, 17726–17737.
21 B. Kumar, T. Kawawaki, N. Shimizu, Y. Imai, D. Suzuki, S. Hossain, L. V. Nair and Y. Negishi, *Nanoscale*, 2020, **12**, 9969–9979.
22 T. Kawawaki and Y. Negishi, *Nanomaterials*, 2020, **10**, 238.
23 T. Kawawaki, Y. Negishi and H. Kawasaki, *Nanoscale Adv.*, 2020, **2**, 17–36.
24 M. Liu, Z. Zhao, X. Duan and Y. Huang, *Adv. Mater.*, 2019, **31**, 1802234.
25 A. Kudo and Y. Miseki, *Chem. Soc. Rev.*, 2009, **38**, 253–278.
26 K. Maeda, *ACS Catal.*, 2013, **3**, 1486–1503.
27 J. Yang, D. Wang, H. Han and C. Li, *Acc. Chem. Res.*, 2013, **46**, 1900–1909.
28 Q. Wang and K. Domen, *Chem. Rev.*, 2020, **120**, 919–985.
29 Y. Wang, H. Suzuki, J. Xie, O. Tomita, D. J. Martin, M. Higashi, D. Kong, R. Abe and J. Tang, *Chem. Rev.*, 2018, **118**, 5201–5241.
30 G. Zhang, Z.-A. Lan, L. Lin, S. Lin and X. Wang, *Chem. Sci.*, 2016, **7**, 3062–3066.
31 X. Li, J. Yu, J. Low, Y. Fang, J. Xiao and X. Chen, *J. Mater. Chem. A*, 2015, **3**, 2485–2534.
32 T. Hisatomi, J. Kubota and K. Domen, *Chem. Soc. Rev.*, 2014, **43**, 7520–7535.
33 Z. Wang, C. Li and K. Domen, *Chem. Soc. Rev.*, 2019, **48**, 2109–2125.
34 X. Chen, S. Shen, L. Guo and S. S. Mao, *Chem. Rev.*, 2010, **110**, 6503–6570.
35 K. Domen, S. Naito, M. Soma, T. Onishi and K. Tamaru, *J. Chem. Soc., Chem. Commun.*, 1980, 543–544.
36 S. Sato and J. M. White, *Chem. Phys. Lett.*, 1980, **72**, 83–86.
37 J. M. Lehn, J. P. Sauvage and R. Ziessel, *Nouv. J. Chim.*, 1980, 623–627.
38 K. Maeda and K. Domen, *J. Phys. Chem. Lett.*, 2010, **1**, 2655–2661.
39 Q. Wang, T. Hisatomi, Q. Jia, H. Tokudome, M. Zhong, C. Wang, Z. Pan, T. Takata, M. Nakabayashi, N. Shibata, Y. Li, I. D. Sharp, A. Kudo, T. Yamada and K. Domen, *Nat. Mater.*, 2016, **15**, 611–615.
40 B. Kraeutler and A. J. Bard, *J. Am. Chem. Soc.*, 1978, **100**, 4317–4318.
41 T. Takata, J. Jiang, Y. Sakata, M. Nakabayashi, N. Shibata, V. Nandal, K. Seki, T. Hisatomi and K. Domen, *Nature*, 2020, **581**, 411–414.
42 Y. Zhu, T. Wang, T. Xu, Y. Li and C. Wang, *Appl. Surf. Sci.*, 2019, **464**, 36–42.

43 K. Maeda, K. Teramura, D. Lu, T. Takata, N. Saito, Y. Inoue and K. Domen, *Nature*, 2006, **440**, 295.

44 T. Pradeep, *NANO: The Essentials: Understanding Nanoscience and Nanotechnology*, McGraw-Hill Education, New York, 2007.

45 K. J. Taylor, C. L. Pettiette-Hall, O. Cheshnovsky and R. E. Smalley, *J. Chem. Phys.*, 1992, **96**, 3319–3329.

46 W. D. Knight, W. A. de Heer and W. A. Saunders, *Z. Phys. D: At., Mol. Clusters*, 1986, **3**, 109–114.

47 T. P. Martin, T. Bergmann, H. Göehlich and T. Lange, *J. Phys. Chem.*, 1991, **95**, 6421–6429.

48 L.-S. Wang, O. Cheshnovsky, R. E. Smalley, J. P. Carpenter and S. J. Hwu, *J. Chem. Phys.*, 1992, **96**, 4028–4031.

49 R. L. Whetten, D. M. Cox, D. J. Trevor and A. Kaldor, *Phys. Rev. Lett.*, 1985, **54**, 1494–1497.

50 S. C. Richtsmeier, E. K. Parks, K. Liu, L. G. Pobo and S. J. Riley, *J. Chem. Phys.*, 1985, **82**, 3659–3665.

51 P. Fayet, F. Granzer, G. Hegenbart, E. Moisar, B. Pischel and L. Wöste, *Z. Phys. D: At., Mol. Clusters*, 1986, **3**, 299–302.

52 A. Nakajima, K. Hoshino, T. Naganuma, Y. Sone and K. Kaya, *J. Chem. Phys.*, 1991, **95**, 7061–7066.

53 H. Zhang, T. Watanabe, M. Okumura, M. Haruta and N. Toshima, *Nat. Mater.*, 2012, **11**, 49–52.

54 K. Kusada, H. Kobayashi, R. Ikeda, Y. Kubota, M. Takata, S. Toh, T. Yamamoto, S. Matsumura, N. Sumi, K. Sato, K. Nagaoka and H. Kitagawa, *J. Am. Chem. Soc.*, 2014, **136**, 1864–1871.

55 Y. Negishi, W. Kurashige, Y. Niihori, T. Iwasa and K. Nobusada, *Phys. Chem. Chem. Phys.*, 2010, **12**, 6219–6225.

56 Y. Negishi, T. Iwai and M. Ide, *Chem. Commun.*, 2010, **46**, 4713–4715.

57 Y. Negishi, R. Arai, Y. Niihori and T. Tsukuda, *Chem. Commun.*, 2011, **47**, 5693–5695.

58 Y. Negishi, K. Igarashi, K. Munakata, W. Ohgake and K. Nobusada, *Chem. Commun.*, 2012, **48**, 660–662.

59 W. Kurashige and Y. Negishi, *J. Cluster Sci.*, 2012, **23**, 365–374.

60 Y. Negishi, U. Kamimura, M. Ide and M. Hirayama, *Nanoscale*, 2012, **4**, 4263–4268.

61 Y. Negishi, K. Munakata, W. Ohgake and K. Nobusada, *J. Phys. Chem. Lett.*, 2012, **3**, 2209–2214.

62 Y. Niihori, W. Kurashige, M. Matsuzaki and Y. Negishi, *Nanoscale*, 2013, **5**, 508–512.

63 Y. Negishi, W. Kurashige, Y. Kobayashi, S. Yamazoe, N. Kojima, M. Seto and T. Tsukuda, *J. Phys. Chem. Lett.*, 2013, **4**, 3579–3583.

64 Y. Negishi, W. Kurashige, Y. Niihori and K. Nobusada, *Phys. Chem. Chem. Phys.*, 2013, **15**, 18736–18751.

65 A. Puls, P. Jerabek, W. Kurashige, M. Förster, M. Molon, T. Bollermann, M. Winter, C. Gemel, Y. Negishi, G. Frenking and R. A. Fischer, *Angew. Chem., Int. Ed.*, 2014, **53**, 4327–4331.

66 D. Bahnemann, A. Henglein, J. Lilie and L. Spanhel, *J. Phys. Chem.*, 1984, **88**, 709–711.

67 H. N. Ghosh, J. B. Asbury and T. Lian, *J. Phys. Chem. B*, 1998, **102**, 6482–6486.

68 B. Ohtani, R. M. Bowman, D. P. Colombo Jr., H. Kominami, H. Noguchi and K. Uosaki, *Chem. Lett.*, 1998, 579–580.

69 A. Yamakata, T.-a. Ishibashi and H. Onishi, *Chem. Phys. Lett.*, 2001, **333**, 271–277.

70 T. Yoshihara, R. Katoh, A. Furube, Y. Tamaki, M. Murai, K. Hara, S. Murata, H. Arakawa and M. Tachiya, *J. Phys. Chem. B*, 2004, **108**, 3817–3823.

71 J. Lee, H. S. Shim, M. Lee, J. K. Song and D. Lee, *J. Phys. Chem. Lett.*, 2011, **2**, 2840–2845.

72 Y. Du, H. Sheng, D. Astruc and M. Zhu, *Chem. Rev.*, 2020, **120**, 526–622.

73 X.-Q. Gong, A. Selloni, O. Dulub, P. Jacobson and U. Diebold, *J. Am. Chem. Soc.*, 2008, **130**, 370–381.

74 M. R. Nellist, F. A. L. Laskowski, J. Qiu, H. Hajibabaei, K. Sivula, T. W. Hamann and S. W. Boettcher, *Nat. Energy*, 2018, **3**, 46–52.

75 M. R. Nellist, J. Qiu, F. A. L. Laskowski, F. M. Toma and S. W. Boettcher, *ACS Energy Lett.*, 2018, **3**, 2286–2291.

76 G. N. Vayssilov, Y. Lykhach, A. Migani, T. Staudt, G. P. Petrova, N. Tsud, T. Skála, A. Bruix, F. Illas, K. C. Prince, V. Matolín, K. M. Neyman and J. Libuda, *Nat. Mater.*, 2011, **10**, 310–315.

77 K. He, J. Xie, Z.-Q. Liu, N. Li, X. Chen, J. Hu and X. Li, *J. Mater. Chem. A*, 2018, **6**, 13110–13122.

78 T. Kawawaki, Y. Mori, K. Wakamatsu, S. Ozaki, M. Kawachi, S. Hossain and Y. Negishi, *J. Mater. Chem. A*, 2020, **8**, 16081–16113.

79 Y. Negishi, K. Nobusada and T. Tsukuda, *J. Am. Chem. Soc.*, 2005, **127**, 5261–5270.

80 M. Agrachev, M. Ruzzi, A. Venzo and F. Maran, *Acc. Chem. Res.*, 2019, **52**, 44–52.

81 K. Kwak and D. Lee, *Acc. Chem. Res.*, 2019, **52**, 12–22.

82 B. Nieto-Ortega and T. Bürgi, *Acc. Chem. Res.*, 2018, **51**, 2811–2819.

83 H. Qian, M. Zhu, Z. Wu and R. Jin, *Acc. Chem. Res.*, 2012, **45**, 1470–1479.

84 N. A. Sakthivel and A. Dass, *Acc. Chem. Res.*, 2018, **51**, 1774–1783.

85 T. Tsukuda and H. Häkkinen, *Protected Metal Clusters: From Fundamentals to Applications*. Elsevier, Amsterdam, 2015.

86 R. L. Whetten, H.-C. Weissker, J. J. Pelayo, S. M. Mullins, X. López-Lozano and I. L. Garzón, *Acc. Chem. Res.*, 2019, **52**, 34–43.

87 T. Tsukuda, *Bull. Chem. Soc. Jpn.*, 2012, **85**, 151–168.

88 B. Bhattarai, Y. Zaker, A. Atnagulov, B. Yoon, U. Landman and T. P. Bigioni, *Acc. Chem. Res.*, 2018, **51**, 3104–3113.

89 Z. Gan, N. Xia and Z. Wu, *Acc. Chem. Res.*, 2018, **51**, 2774–2783.

90 A. Ghosh, O. F. Mohammed and O. M. Bakr, *Acc. Chem. Res.*, 2018, **51**, 3094–3103.

91 S. Hossain, Y. Niihori, L. V. Nair, B. Kumar, W. Kurashige and Y. Negishi, *Acc. Chem. Res.*, 2018, **51**, 3114–3124.

92 J. Yan, B. K. Teo and N. Zheng, *Acc. Chem. Res.*, 2018, **51**, 3084–3093.

93 T. Kawawaki, Y. Imai, D. Suzuki, S. Kato, I. Kobayashi, T. Suzuki, R. Kaneko, S. Hossain and Y. Negishi, *Chem. – Eur. J.*, 2020, **26**, 16150–16193.

94 X. Kang, Y. Li, M. Zhu and R. Jin, *Chem. Soc. Rev.*, 2020, **49**, 6443–6514.

95 S. Bhat, A. Baksi, S. K. Mudedla, G. Natarajan, V. Subramanian and T. Pradeep, *J. Phys. Chem. Lett.*, 2017, **8**, 2787–2793.

96 S. Tian, L. Liao, J. Yuan, C. Yao, J. Chen, J. Yang and Z. Wu, *Chem. Commun.*, 2016, **52**, 9873–9876.

97 S. Yamazoe, W. Kurashige, K. Nobusada, Y. Negishi and T. Tsukuda, *J. Phys. Chem. C*, 2014, **118**, 25284–25290.

98 C. Kumara, C. M. Aikens and A. Dass, *J. Phys. Chem. Lett.*, 2014, **5**, 461–466.

99 C. Yao, Y.-j. Lin, J. Yuan, L. Liao, M. Zhu, L.-h. Weng, J. Yang and Z. Wu, *J. Am. Chem. Soc.*, 2015, **137**, 15350–15353.

100 W. Fei, S. Antonello, T. Dainese, A. Dolmella, M. Lahtinen, K. Rissanen, A. Venzo and F. Maran, *J. Am. Chem. Soc.*, 2019, **141**, 16033–16045.

101 C. Sun, N. Mammen, S. Kaappa, P. Yuan, G. Deng, C. Zhao, J. Yan, S. Malola, K. Honkala, H. Häkkinen, B. K. Teo and N. Zheng, *ACS Nano*, 2019, **13**, 5975–5986.

102 S. Lee, M. S. Bootharaju, G. Deng, S. Malola, W. Baek, H. Häkkinen, N. Zheng and T. Hyeon, *J. Am. Chem. Soc.*, 2020, **142**, 13974–13981.

103 W. Kurashige, S. Yamazoe, M. Yamaguchi, K. Nishido, K. Nobusada, T. Tsukuda and Y. Negishi, *J. Phys. Chem. Lett.*, 2014, **5**, 2072–2076.

104 S. Sharma, W. Kurashige, K. Nobusada and Y. Negishi, *Nanoscale*, 2015, **7**, 10606–10612.

105 Y. Niihori, M. Eguro, A. Kato, S. Sharma, B. Kumar, W. Kurashige, K. Nobusada and Y. Negishi, *J. Phys. Chem. C*, 2016, **120**, 14301–14309.

106 Y. Niihori, S. Hossain, B. Kumar, L. V. Nair, W. Kurashige and Y. Negishi, *APL Mater.*, 2017, **5**, 053201.

107 L. V. Nair, S. Hossain, S. Takagi, Y. Imai, G. Hu, S. Wakayama, B. Kumar, W. Kurashige, D.-e. Jiang and Y. Negishi, *Nanoscale*, 2018, **10**, 18969–18979.

108 S. Hossain, Y. Imai, D. Suzuki, W. Choi, Z. Chen, T. Suzuki, M. Yoshioka, T. Kawawaki, D. Lee and Y. Negishi, *Nanoscale*, 2019, **11**, 22089–22098.

109 S. Hossain, Y. Imai, Y. Motohashi, Z. Chen, D. Suzuki, T. Suzuki, Y. Kataoka, M. Hirata, T. Ono, W. Kurashige, T. Kawawaki, T. Yamamoto and Y. Negishi, *Mater. Horiz.*, 2020, **7**, 796–803.

110 S. Hossain, T. Ono, M. Yoshioka, G. Hu, M. Hosoi, Z. Chen, L. V. Nair, Y. Niihori, W. Kurashige, D.-e. Jiang and Y. Negishi, *J. Phys. Chem. Lett.*, 2018, **9**, 2590–2594.

111 P. D. Jadzinsky, G. Calero, C. J. Ackerson, D. A. Bushnell and R. D. Kornberg, *Science*, 2007, **318**, 430–433.

112 M. Zhu, C. M. Aikens, F. J. Hollander, G. C. Schatz and R. Jin, *J. Am. Chem. Soc.*, 2008, **130**, 5883–5885.

113 C. P. Joshi, M. S. Bootharaju, M. J. Alhilaly and O. M. Bakr, *J. Am. Chem. Soc.*, 2015, **137**, 11578–11581.

114 H. Yang, Y. Wang, H. Huang, L. Gell, L. Lehtovaara, S. Malola, H. Häkkinen and N. Zheng, *Nat. Commun.*, 2013, **4**, 2422.

115 Y. Negishi, W. Kurashige and U. Kamimura, *Langmuir*, 2011, **27**, 12289–12292.

116 W. Kurashige, M. Yamaguchi, K. Nobusada and Y. Negishi, *J. Phys. Chem. Lett.*, 2012, **3**, 2649–2652.

117 W. Kurashige, K. Munakata, K. Nobusada and Y. Negishi, *Chem. Commun.*, 2013, **49**, 5447–5449.

118 W. Kurashige, S. Yamazoe, K. Kanehira, T. Tsukuda and Y. Negishi, *J. Phys. Chem. Lett.*, 2013, **4**, 3181–3185.

119 W. Kurashige, Y. Niihori, S. Sharma and Y. Negishi, *J. Phys. Chem. Lett.*, 2014, **5**, 4134–4142.

120 S. Hossain, W. Kurashige, S. Wakayama, B. Kumar, L. V. Nair, Y. Niihori and Y. Negishi, *J. Phys. Chem. C*, 2016, **120**, 25861–25869.

121 Y. Niihori, S. Hossain, S. Sharma, B. Kumar, W. Kurashige and Y. Negishi, *Chem. Rec.*, 2017, **17**, 473–484.

122 X. Kang and M. Zhu, *Small*, 2019, **15**, 1902703.

123 Z. Lei, X.-K. Wan, S.-F. Yuan, Z.-J. Guan and Q.-M. Wang, *Acc. Chem. Res.*, 2018, **51**, 2465–2474.

124 J.-J. Li, Z.-J. Guan, Z. Lei, F. Hu and Q.-M. Wang, *Angew. Chem., Int. Ed.*, 2019, **58**, 1083–1087.

125 K. Yamamoto, T. Imaoka, M. Tanabe and T. Kambe, *Chem. Rev.*, 2020, **120**, 1397–1437.

126 C. E. Briant, B. R. C. Theobald, J. W. White, L. K. Bell, D. M. P. Mingos and A. J. Welch, *J. Chem. Soc., Chem. Commun.*, 1981, 201–202.

127 M. McPartlin, R. Mason and L. Malatesta, *J. Chem. Soc. D*, 1969, 334.

128 E. G. Mednikov and L. F. Dahl, *Philos. Trans. R. Soc., A*, 2010, **368**, 1301–1332.

129 G. Schmid, *Chem. Rev.*, 1992, **92**, 1709–1727.

130 M. Schulz-Dobrick and M. Jansen, *Z. Anorg. Allg. Chem.*, 2007, **633**, 2326–2331.

131 B. K. Teo, X. Shi and H. Zhang, *J. Am. Chem. Soc.*, 1992, **114**, 2743–2745.

132 J. D. Roth, G. J. Lewis, L. K. Safford, X. Jiang, L. F. Dahl and M. J. Weaver, *J. Am. Chem. Soc.*, 1992, **114**, 6159–6169.

133 A. Ceriotti, N. Masciocchi, P. Macchi and G. Longoni, *Angew. Chem., Int. Ed.*, 1999, **38**, 3724–3727.

134 I. Ciabatti, C. Femoni, M. C. Iapalucci, G. Longoni and S. Zacchini, *J. Cluster Sci.*, 2014, **25**, 115–146.

135 S. S. Kurasov, N. K. Eremenko, Y. L. Slovokhotov and Y. T. Struchkov, *J. Organomet. Chem.*, 1989, **361**, 405–408.

136 L. Hao, G. J. Spivak, J. Xiao, J. J. Vittal and R. J. Puddephatt, *J. Am. Chem. Soc.*, 1995, **117**, 7011–7012.

137 E. Cattabriga, I. Ciabatti, C. Femoni, T. Funaioli, M. C. Iapalucci and S. Zacchini, *Inorg. Chem.*, 2016, **55**, 6068–6079.

138 C. Cesari, I. Ciabatti, C. Femoni, M. C. Iapalucci, F. Mancini and S. Zacchini, *Inorg. Chem.*, 2017, **56**, 1655–1668.

139 L. V. Nair, S. Hossain, S. Wakayama, S. Takagi, M. Yoshioka, J. Maekawa, A. Harasawa, B. Kumar, Y. Niihori, W. Kurashige and Y. Negishi, *J. Phys. Chem. C*, 2017, **121**, 11002–11009.

140 Y. Shichibu and K. Konishi, *Small*, 2010, **6**, 1216–1220.

141 H. Hirai, S. Takano, T. Nakamura and T. Tsukuda, *Inorg. Chem.*, DOI: 10.1021/acs.inorgchem.0c00879.

142 K. Konishi, M. Iwasaki and Y. Shichibu, *Acc. Chem. Res.*, 2018, **51**, 3125–3133.

143 B. K. Teo and H. Zhang, *Proc. Natl. Acad. Sci. U. S. A.*, 1991, **88**, 5067–5071.

144 Y. Liu, H. Tsunoyama, T. Akita, S. Xie and T. Tsukuda, *ACS Catal.*, 2011, **1**, 2–6.

145 S. Xie, H. Tsunoyama, W. Kurashige, Y. Negishi and T. Tsukuda, *ACS Catal.*, 2012, **2**, 1519–1523.

146 N. Sakamoto, H. Ohtsuka, T. Ikeda, K. Maeda, D. Lu, M. Kanehara, K. Teramura, T. Teranishi and K. Domen, *Nanoscale*, 2009, **1**, 106–109.

147 Y. Negishi, *Bull. Chem. Soc. Jpn.*, 2014, **87**, 375–389.

148 W. Kurashige, Y. Niihori, S. Sharma and Y. Negishi, *Coord. Chem. Rev.*, 2016, **320–321**, 238–250.

149 V. G. Albano, P. L. Bellon, M. Manassero and M. Sansoni, *J. Chem. Soc. D*, 1970, 1210–1211.

150 G. Schmid, R. Pfeil, R. Boese, F. Bandermann, S. Meyer, G. H. M. Calis and J. W. A. van der Velden, *Chem. Ber.*, 1981, **114**, 3634–3642.

151 P. Chini, *J. Organomet. Chem.*, 1980, **200**, 37–61.

152 M. Paolieri, I. Ciabatti and M. Fontani, *J. Cluster Sci.*, 2019, **30**, 1623–1631.

153 R. Jin, C. Zeng, M. Zhou and Y. Chen, *Chem. Rev.*, 2016, **116**, 10346–10413.

154 I. Chakraborty and T. Pradeep, *Chem. Rev.*, 2017, **117**, 8208–8271.

155 A. Ebina, S. Hossain, H. Horihata, S. Ozaki, S. Kato, T. Kawawaki and Y. Negishi, *Nanomaterials*, 2020, **10**, 1105.

156 Y. Niihori, K. Yoshida, S. Hossain, W. Kurashige and Y. Negishi, *Bull. Chem. Soc. Jpn.*, 2019, **92**, 664–695.

157 X. Kang, H. Chong and M. Zhu, *Nanoscale*, 2018, **10**, 10758–10834.

158 X. Kang and M. Zhu, *Chem. Mater.*, 2019, **31**, 9939–9969.

159 X. Kang and M. Zhu, *Coord. Chem. Rev.*, 2019, **394**, 1–38.

160 X. Kang and M. Zhu, *Chem. Soc. Rev.*, 2019, **48**, 2422–2457.

161 H. Yu, B. Rao, W. Jiang, S. Yang and M. Zhu, *Coord. Chem. Rev.*, 2019, **378**, 595–617.

162 M. Brust, M. Walker, D. Bethell, D. J. Schiffrin and R. Whyman, *J. Chem. Soc., Chem. Commun.*, 1994, 801–802.

163 T. G. Schaaff, G. Knight, M. N. Shafigullin, R. F. Borkman and R. L. Whetten, *J. Phys. Chem. B*, 1998, **102**, 10643–10646.

164 S. Kumar, M. D. Bolan and T. P. Bigioni, *J. Am. Chem. Soc.*, 2010, **132**, 13141–13143.

165 K. Kimura, N. Sugimoto, S. Sato, H. Yao, Y. Negishi and T. Tsukuda, *J. Phys. Chem. C*, 2009, **113**, 14076–14082.

166 Y. Yu, Z. Luo, D. M. Chevrier, D. T. Leong, P. Zhang, D.-e. Jiang and J. Xie, *J. Am. Chem. Soc.*, 2014, **136**, 1246–1249.

167 C. Gautier and T. Bürgi, *J. Am. Chem. Soc.*, 2006, **128**, 11079–11087.

168 Y. Negishi, S. Hashimoto, A. Ebina, K. Hamada, S. Hossain and T. Kawawaki, *Nanoscale*, 2020, **12**, 8017–8039.

169 V. L. Jimenez, M. C. Leopold, C. Mazzitelli, J. W. Jorgenson and R. W. Murray, *Anal. Chem.*, 2003, **75**, 199–206.

170 S. Knoppe and P. Vogt, *Anal. Chem.*, 2019, **91**, 1603–1609.

171 Y. Negishi, T. Nakazaki, S. Malola, S. Takano, Y. Niihori, W. Kurashige, S. Yamazoe, T. Tsukuda and H. Häkkinen, *J. Am. Chem. Soc.*, 2015, **137**, 1206–1212.

172 Y. Negishi, C. Sakamoto, T. Ohyama and T. Tsukuda, *J. Phys. Chem. Lett.*, 2012, **3**, 1624–1628.

173 D. M. Black, S. B. H. Bach and R. L. Whetten, *Anal. Chem.*, 2016, **88**, 5631–5636.

174 D. M. Black, N. Bhattarai, S. B. H. Bach and R. L. Whetten, *J. Phys. Chem. Lett.*, 2016, **7**, 3199–3205.

175 Y. Niihori, M. Matsuzaki, T. Pradeep and Y. Negishi, *J. Am. Chem. Soc.*, 2013, **135**, 4946–4949.

176 Y. Niihori, M. Matsuzaki, C. Uchida and Y. Negishi, *Nanoscale*, 2014, **6**, 7889–7896.

177 Y. Niihori, Y. Kikuchi, A. Kato, M. Matsuzaki and Y. Negishi, *ACS Nano*, 2015, **9**, 9347–9356.

178 Y. Niihori, C. Uchida, W. Kurashige and Y. Negishi, *Phys. Chem. Chem. Phys.*, 2016, **18**, 4251–4265.

179 Y. Niihori, Y. Kikuchi, D. Shima, C. Uchida, S. Sharma, S. Hossain, W. Kurashige and Y. Negishi, *Ind. Eng. Chem. Res.*, 2017, **56**, 1029–1035.

180 Y. Niihori, D. Shima, K. Yoshida, K. Hamada, L. V. Nair, S. Hossain, W. Kurashige and Y. Negishi, *Nanoscale*, 2018, **10**, 1641–1649.

181 Y. Niihori, Y. Koyama, S. Watanabe, S. Hashimoto, S. Hossain, L. V. Nair, B. Kumar, W. Kurashige and Y. Negishi, *J. Phys. Chem. Lett.*, 2018, **9**, 4930–4934.

182 Y. Niihori, S. Hashimoto, Y. Koyama, S. Hossain, W. Kurashige and Y. Negishi, *J. Phys. Chem. C*, 2019, **123**, 13324–13329.

183 A. Ghosh, J. Hassinen, P. Pulkkinen, H. Tenhu, R. H. A. Ras and T. Pradeep, *Anal. Chem.*, 2014, **86**, 12185–12190.

184 C. Yao, J. Chen, M.-B. Li, L. Liu, J. Yang and Z. Wu, *Nano Lett.*, 2015, **15**, 1281–1287.

185 S. Hossain, D. Suzuki, T. Iwasa, R. Kaneko, T. Suzuki, S. Miyajima, Y. Iwamatsu, S. Pollitt, T. Kawawaki, N. Barrabés, G. Rupprechter and Y. Negishi, *J. Phys. Chem. C*, 2020, **124**, 22304–22313.

186 T. G. Schaaff and R. L. Whetten, *J. Phys. Chem. B*, 1999, **103**, 9394–9396.

187 Y. Shichibu, Y. Negishi, T. Tsukuda and T. Teranishi, *J. Am. Chem. Soc.*, 2005, **127**, 13464–13465.

188 A. C. Dharmaratne, T. Krick and A. Dass, *J. Am. Chem. Soc.*, 2009, **131**, 13604–13605.
189 Q. Yao, X. Yuan, V. Fung, Y. Yu, D. T. Leong, D.-e. Jiang and J. Xie, *Nat. Commun.*, 2017, **8**, 927.
190 T. Chen, V. Fung, Q. Yao, Z. Luo, D.-e. Jiang and J. Xie, *J. Am. Chem. Soc.*, 2018, **140**, 11370–11377.
191 Q. Yao, T. Chen, X. Yuan and J. Xie, *Acc. Chem. Res.*, 2018, **51**, 1338–1348.
192 S. Takano, S. Yamazoe, K. Koyasu and T. Tsukuda, *J. Am. Chem. Soc.*, 2015, **137**, 7027–7030.
193 C. Zeng, Y. Chen, A. Das and R. Jin, *J. Phys. Chem. Lett.*, 2015, **6**, 2976–2986.
194 S. Takano, S. Ito and T. Tsukuda, *J. Am. Chem. Soc.*, 2019, **141**, 15994–16002.
195 S. Wang, X. Meng, A. Das, T. Li, Y. Song, T. Cao, X. Zhu, M. Zhu and R. Jin, *Angew. Chem., Int. Ed.*, 2014, **53**, 2376–2380.
196 L. Liao, S. Zhou, Y. Dai, L. Liu, C. Yao, C. Fu, J. Yang and Z. Wu, *J. Am. Chem. Soc.*, 2015, **137**, 9511–9514.
197 S. Wang, Y. Song, S. Jin, X. Liu, J. Zhang, Y. Pei, X. Meng, M. Chen, P. Li and M. Zhu, *J. Am. Chem. Soc.*, 2015, **137**, 4018–4021.
198 K. R. Krishnadas, A. Baksi, A. Ghosh, G. Natarajan and T. Pradeep, *Nat. Commun.*, 2016, **7**, 13447.
199 R. Kazan, U. Müller and T. Bürgi, *Nanoscale*, 2019, **11**, 2938–2945.
200 Y. Li, M. Chen, S. Wang and M. Zhu, *Nanomaterials*, 2018, **8**, 1070.
201 R. Kazan, B. Zhang and T. Bürgi, *Dalton Trans.*, 2017, **46**, 7708–7713.
202 S. Yang, J. Chai, Y. Song, J. Fan, T. Chen, S. Wang, H. Yu, X. Li and M. Zhu, *J. Am. Chem. Soc.*, 2017, **139**, 5668–5671.
203 R. L. Whetten, M. N. Shafigullin, J. T. Khoury, T. G. Schaaff, I. Vezmar, M. M. Alvarez and A. Wilkinson, *Acc. Chem. Res.*, 1999, **32**, 397–406.
204 H. Häkkinen, M. Walter and H. Grönbeck, *J. Phys. Chem. B*, 2006, **110**, 9927–9931.
205 R. L. Whetten and R. C. Price, *Science*, 2007, **318**, 407–408.
206 Y. Song, S. Wang, J. Zhang, X. Kang, S. Chen, P. Li, H. Sheng and M. Zhu, *J. Am. Chem. Soc.*, 2014, **136**, 2963–2965.
207 J. Zhong, X. Tang, J. Tang, J. Su and Y. Pei, *J. Phys. Chem. C*, 2015, **119**, 9205–9214.
208 X.-K. Wan, Q. Tang, S.-F. Yuan, D.-e. Jiang and Q.-M. Wang, *J. Am. Chem. Soc.*, 2015, **137**, 652–655.
209 S. Ito, S. Takano and T. Tsukuda, *J. Phys. Chem. Lett.*, 2019, **10**, 6892–6896.
210 Y. Miseki, H. Kato and A. Kudo, *Energy Environ. Sci.*, 2009, **2**, 306–314.
211 K. Maeda and K. Domen, *Chem. Mater.*, 2010, **22**, 612–623.
212 T. Tomio, H. Miki, H. Tabata, T. Kawai and S. Kawai, *J. Appl. Phys.*, 1994, **76**, 5886–5890.
213 T. Puangpetch, S. Chavadej and T. Sreethawong, *Energy Convers. Manage.*, 2011, **52**, 2256–2261.
214 R. Abe, *Bull. Chem. Soc. Jpn.*, 2011, **84**, 1000–1030.
215 Y. Miseki, S. Fujiyoshi, T. Gunji and K. Sayama, *J. Phys. Chem. C*, 2017, **121**, 9691–9697.
216 F. E. Osterloh, *Chem. Mater.*, 2008, **20**, 35–54.
217 A. Iwase, Y. H. Ng, Y. Ishiguro, A. Kudo and R. Amal, *J. Am. Chem. Soc.*, 2011, **133**, 11054–11057.
218 K. Maeda, N. Sakamoto, T. Ikeda, H. Ohtsuka, A. Xiong, D. Lu, M. Kanehara, T. Teranishi and K. Domen, *Chem. – Eur. J.*, 2010, **16**, 7750–7759.
219 T. Ikeda, A. Xiong, T. Yoshinaga, K. Maeda, K. Domen and T. Teranishi, *J. Phys. Chem. C*, 2013, **117**, 2467–2473.
220 K. Maeda, A. Xiong, T. Yoshinaga, T. Ikeda, N. Sakamoto, T. Hisatomi, M. Takashima, D. Lu, M. Kanehara, T. Setoyama, T. Teranishi and K. Domen, *Angew. Chem., Int. Ed.*, 2010, **49**, 4096–4099.
221 A. Xiong, T. Yoshinaga, T. Ikeda, M. Takashima, T. Hisatomi, K. Maeda, T. Setoyama, T. Teranishi and K. Domen, *Eur. J. Inorg. Chem.*, 2014, 767–772.
222 T. Yoshinaga, M. Saruyama, A. Xiong, Y. Ham, Y. Kuang, R. Niishiro, S. Akiyama, M. Sakamoto, T. Hisatomi, K. Domen and T. Teranishi, *Nanoscale*, 2018, **10**, 10420–10427.
223 Y. Shichibu, Y. Negishi, H. Tsunoyama, M. Kanehara, T. Teranishi and T. Tsukuda, *Small*, 2007, **3**, 835–839.
224 K. Nakata, S. Sugawara, W. Kurashige, Y. Negishi, M. Nagata, S. Uchida, C. Terashima, T. Kondo, M. Yuasa and A. Fujishima, *Int. J. Photoenergy*, 2013, **2013**, 456583.
225 Y. Negishi, M. Mizuno, M. Hirayama, M. Omatoi, T. Takayama, A. Iwase and A. Kudo, *Nanoscale*, 2013, **5**, 7188–7192.
226 N. W. Pirie and K. G. Pinhey, *J. Biol. Chem.*, 1929, **84**, 321–333.
227 J. Akola, M. Walter, R. L. Whetten, H. Häkkinen and H. Grönbeck, *J. Am. Chem. Soc.*, 2008, **130**, 3756–3757.
228 M. Walter, J. Akola, O. Lopez-Acevedo, P. D. Jadzinsky, G. Calero, C. J. Ackerson, R. L. Whetten, H. Grönbeck and H. Häkkinen, *Proc. Natl. Acad. Sci. U. S. A.*, 2008, **105**, 9157–9162.
229 C. M. Aikens, *J. Phys. Chem. C*, 2008, **112**, 19797–19800.
230 D.-e. Jiang, M. Kühn, Q. Tang and F. Weigend, *J. Phys. Chem. Lett.*, 2014, **5**, 3286–3289.
231 W. Kurashige, R. Kumazawa, Y. Mori and Y. Negishi, *J. Mater. Appl.*, 2018, **7**, 1–11.
232 Y. Negishi, Y. Matsuura, R. Tomizawa, W. Kurashige, Y. Niihori, T. Takayama, A. Iwase and A. Kudo, *J. Phys. Chem. C*, 2015, **119**, 11224–11232.
233 W. Kurashige, R. Hayashi, K. Wakamatsu, Y. Kataoka, S. Hossain, A. Iwase, A. Kudo, S. Yamazoe and Y. Negishi, *ACS Appl. Energy Mater.*, 2019, **2**, 4175–4187.
234 M. P. Johansson, A. Lechtken, D. Schooss, M. M. Kappes and F. Furche, *Phys. Rev. A: At., Mol., Opt. Phys.*, 2008, **77**, 053202.
235 S. Gilb, P. Weis, F. Furche, R. Ahlrichs and M. M. Kappes, *J. Chem. Phys.*, 2002, **116**, 4094–4101.
236 A. Lechtken, C. Neiss, M. M. Kappes and D. Schooss, *Phys. Chem. Chem. Phys.*, 2009, **11**, 4344–4350.
237 W. Huang and L.-S. Wang, *Phys. Rev. Lett.*, 2009, **102**, 153401.
238 H. Häkkinen, B. Yoon, U. Landman, X. Li, H.-J. Zhai and L.-S. Wang, *J. Phys. Chem. A*, 2003, **107**, 6168–6175.
239 H. Häkkinen and U. Landman, *Phys. Rev. B: Condens. Matter Mater. Phys.*, 2000, **62**, R2287–R2290.
240 D.-e. Jiang, S. H. Overbury and S. Dai, *J. Phys. Chem. Lett.*, 2011, **2**, 1211–1215.
241 G. Zanti and D. Peeters, *J. Phys. Chem. A*, 2010, **114**, 10345–10356.
242 H. K. Yuan, A. L. Kuang, C. L. Tian and H. Chen, *AIP Adv.*, 2014, **4**, 037107.
243 Y.-R. Luo, *Comprehensive Handbook of Chemical Bond Energies*, CRC Press, Boca Raton, Florida, 2007.
244 L. Vitos, A. V. Ruban, H. L. Skriver and J. Kollár, *Surf. Sci.*, 1998, **411**, 186–202.
245 R. Konta, T. Ishii, H. Kato and A. Kudo, *J. Phys. Chem. B*, 2004, **108**, 8992–8995.
246 K. Iizuka, T. Wato, Y. Miseki, K. Saito and A. Kudo, *J. Am. Chem. Soc.*, 2011, **133**, 20863–20868.
247 W. Kurashige, R. Kumazawa, D. Ishii, R. Hayashi, Y. Niihori, S. Hossain, L. V. Nair, T. Takayama, A. Iwase, S. Yamazoe, T. Tsukuda, A. Kudo and Y. Negishi, *J. Phys. Chem. C*, 2018, **122**, 13669–13681.
248 A. A. Melvin, K. Illath, T. Das, T. Raja, S. Bhattacharyya and C. S. Gopinath, *Nanoscale*, 2015, **7**, 13477–13488.
249 S.-F. Hung, Y.-C. Yu, N.-T. Suen, G.-Q. Tzeng, C.-W. Tung, Y.-Y. Hsu, C.-S. Hsu, C.-K. Chang, T.-S. Chan, H.-S. Sheu, J.-F. Lee and H. M. Chen, *Chem. Commun.*, 2016, **52**, 1567–1570.
250 H. Bian, N. T. Nguyen, J. Yoo, S. Hejazi, S. Mohajernia, J. Müller, E. Spiecker, H. Tsuchiya, O. Tomanec, B. E. Sanabria-Arenas, R. Zboril, Y. Y. Li and P. Schmuki, *ACS Appl. Mater. Interfaces*, 2018, **10**, 18220–18226.
251 K. Maeda and K. Domen, *J. Phys. Chem. C*, 2007, **111**, 7851–7861.
252 K. Maeda, *J. Photochem. Photobiol., C*, 2011, **12**, 237–268.
253 K. Maeda, D. Lu and K. Domen, *Chem. – Eur. J.*, 2013, **19**, 4986–4991.
254 K. Maeda, K. Teramura, D. Lu, N. Saito, Y. Inoue and K. Domen, *Angew. Chem., Int. Ed.*, 2006, **45**, 7806–7809.
255 M. Yoshida, K. Takanabe, K. Maeda, A. Ishikawa, J. Kubota, Y. Sakata, Y. Ikezawa and K. Domen, *J. Phys. Chem. C*, 2009, **113**, 10151–10157.
256 K. Maeda, K. Teramura, D. Lu, N. Saito, Y. Inoue and K. Domen, *J. Phys. Chem. C*, 2007, **111**, 7554–7560.
257 S. J. Tauster, S. C. Fung and R. L. Garten, *J. Am. Chem. Soc.*, 1978, **100**, 170–175.
258 S. J. Tauster, *Acc. Chem. Res.*, 1987, **20**, 389–394.

259 E. J. Braunschweig, A. D. Logan, A. K. Datye and D. J. Smith, *J. Catal.*, 1989, **118**, 227–237.

260 A. D. Logan, E. J. Braunschweig, A. K. Datye and D. J. Smith, *Langmuir*, 1988, **4**, 827–830.

261 S. Labich, E. Taglauer and H. Knözinger, *Top. Catal.*, 2001, **14**, 153–161.

262 L. Liu, C. Ge, W. Zou, X. Gu, F. Gao and L. Dong, *Phys. Chem. Chem. Phys.*, 2015, **17**, 5133–5140.

263 X. Liu, M.-H. Liu, Y.-C. Luo, C.-Y. Mou, S. D. Lin, H. Cheng, J.-M. Chen, J.-F. Lee and T.-S. Lin, *J. Am. Chem. Soc.*, 2012, **134**, 10251–10258.

264 H. Tang, J. Wei, F. Liu, B. Qiao, X. Pan, L. Li, J. Liu, J. Wang and T. Zhang, *J. Am. Chem. Soc.*, 2016, **138**, 56–59.

265 S. Trasatti, *J. Electroanal. Chem. Interfacial Electrochem.*, 1972, **39**, 163–184.

266 T. Hisatomi, K. Maeda, K. Takanabe, J. Kubota and K. Domen, *J. Phys. Chem. C*, 2009, **113**, 21458–21466.

267 K. Maeda, K. Teramura, H. Masuda, T. Takata, N. Saito, Y. Inoue and K. Domen, *J. Phys. Chem. B*, 2006, **110**, 13107–13112.

268 T. Ohno, L. Bai, T. Hisatomi, K. Maeda and K. Domen, *J. Am. Chem. Soc.*, 2012, **134**, 8254–8259.

269 K. Maeda, D. Lu, K. Teramura and K. Domen, *Energy Environ. Sci.*, 2010, **3**, 471–478.

270 W. Kurashige, Y. Mori, S. Ozaki, M. Kawachi, S. Hossain, T. Kawawaki, C. J. Shearer, A. Iwase, G. F. Metha, S. Yamazoe, A. Kudo and Y. Negishi, *Angew. Chem., Int. Ed.*, 2020, **59**, 7076–7082.

271 Y. Sakata, T. Hayashi, R. Yasunaga, N. Yanaga and H. Imamura, *Chem. Commun.*, 2015, **51**, 12935–12938.

272 T. H. Chiang, H. Lyu, T. Hisatomi, Y. Goto, T. Takata, M. Katayama, T. Minegishi and K. Domen, *ACS Catal.*, 2018, **8**, 2782–2788.

273 H. Kato and A. Kudo, *J. Phys. Chem. B*, 2001, **105**, 4285–4292.

274 J. Ji, G. Wang, T. Wang, X. You and X. Xu, *Nanoscale*, 2014, **6**, 9185–9191.

275 R. Li, F. Zhang, D. Wang, J. Yang, M. Li, J. Zhu, X. Zhou, H. Han and C. Li, *Nat. Commun.*, 2013, **4**, 1432.

276 R. Takahata, S. Yamazoe, Y. Maehara, K. Yamazaki, S. Takano, W. Kurashige, Y. Negishi, K. Gohara and T. Tsukuda, *J. Phys. Chem. C*, 2020, **124**, 6907–6912.

277 H. Asakura, S. Hosokawa, T. Ina, K. Kato, K. Nitta, K. Uera, T. Uruga, H. Miura, T. Shishido, J. Ohyama, A. Satsuma, K. Sato, A. Yamamoto, S. Hinokuma, H. Yoshida, M. Machida, S. Yamazoe, T. Tsukuda, K. Teramura and T. Tanaka, *J. Am. Chem. Soc.*, 2018, **140**, 176–184.

278 S. Tian, S. Cao, T. Chen, S. Zang and J. Xie, *Chem. Commun.*, 2020, **56**, 1163–1174.

279 Y. H. Li, J. Xing, X. H. Yang and H. G. Yang, *Chem. – Eur. J.*, 2014, **20**, 12377–12380.

280 J. Xing, J. F. Chen, Y. H. Li, W. T. Yuan, Y. Zhou, L. R. Zheng, H. F. Wang, P. Hu, Y. Wang, H. J. Zhao, Y. Wang and H. G. Yang, *Chem. – Eur. J.*, 2014, **20**, 2138–2144.

281 X. Li, W. Bi, L. Zhang, S. Tao, W. Chu, Q. Zhang, Y. Luo, C. Wu and Y. Xie, *Adv. Mater.*, 2016, **28**, 2427–2431.

282 J. Chen, L. Liu, X. Liu, L. Liao, S. Zhuang, S. Zhou, J. Yang and Z. Wu, *Chem. – Eur. J.*, 2017, **23**, 18187–18192.

283 S. R. Biltek, S. Mandal, A. Sen, A. C. Reber, A. F. Pedicini and S. N. Khanna, *J. Am. Chem. Soc.*, 2013, **135**, 26–29.

284 S. R. Biltek, A. Sen, A. F. Pedicini, A. C. Reber and S. N. Khanna, *J. Phys. Chem. A*, 2014, **118**, 8314–8319.

285 S. R. Biltek, A. C. Reber, S. N. Khanna and A. Sen, *J. Phys. Chem. A*, 2017, **121**, 5324–5331.

286 X. L. Du, X. L. Wang, Y. H. Li, Y. L. Wang, J. J. Zhao, L. J. Fang, L. R. Zheng, H. Tong and H. G. Yang, *Chem. Commun.*, 2017, **53**, 9402–9405.

287 J. Schneider, M. Matsuoka, M. Takeuchi, J. Zhang, Y. Horiuchi, M. Anpo and D. W. Bahnemann, *Chem. Rev.*, 2014, **114**, 9919–9986.